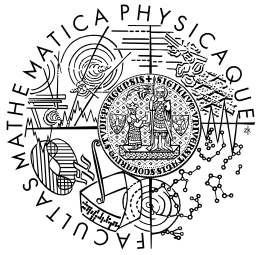

FACULTY
OF MATHEMATICS
AND PHYSICS
Charles University

MASTER THESIS

Martin Krivoš

Study of charmonia production in proton-proton and heavy-ion collisions at the LHC

Institute of Particle and Nuclear Physics

Supervisor of the master thesis:	doc. Mgr. Martin Spousta, Ph.D.
Study programme:	Physics
Study branch:	Nuclear and Subnuclear Physics

Prague 2018

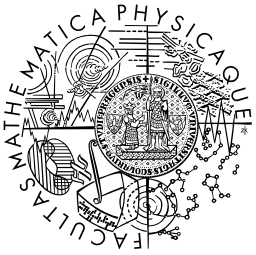

MATEMATICKO-FYZIKÁLNÍ FAKULTA
Univerzita Karlova

DIPLOMOVÁ PRÁCE

Martin Krivoš

Studium produkce charmonií v proton-protonových a těžko-iontových srážkách na LHC

Ústav částicové a jaderné fyziky

Vedoucí diplomové práce:	doc. Mgr. Martin Spousta, Ph.D.
Studijní program:	Fyzika
Studijní obor:	Jaderná a subjaderná fyzika

Praha 2018

I declare that I carried out this master thesis independently, and only with the cited sources, literature and other professional sources.

I understand that my work relates to the rights and obligations under the Act No. 121/2000 Sb., the Copyright Act, as amended, in particular the fact that the Charles University has the right to conclude a license agreement on the use of this work as a school work pursuant to Section 60 subsection 1 of the Copyright Act.

In ..... date ..... signature of the author

I would like to thank my supervisor doc. Mgr. Martin Spousta, Ph.D. for his leadership, patience and his countless contributions to my work.

Title: Study of charmonia production in proton-proton and heavy-ion collisions at the LHC

Author: Martin Krivoš

Ustav: Institute of Particle and Nuclear Physics

Supervisor: doc. Mgr. Martin Spousta, Ph.D., Institute of Particle and Nuclear Physics

Abstract: In this thesis a production of J/ψ meson in pp and heavy-ion collisions was investigated. A comparison between Monte Carlo generator and data by ATLAS experiment at CERN was done. PYTHIA version 8.2 was chosen for the Monte Carlo generator. In the first part, comparisons of several configurations of PYTHIA were used to establish the best matching of the Monte Carlo to the data using collisions with centre-of-mass energy of 7 TeV. Choice of parton distribution functions was found not to be important, while presence or absence of initial and final state radiation were proven to have an important impact on the result. In the second part, correlation of J/ψ meson and the jet production was quantified. Anti-k_t algorithm with $R = 0.4$ was used to reconstruct jets. Pairs of muons were used to identify J/ψ meson candidates. Only less than 10% of J/ψ mesons were found to be associated with jets.

Keywords: charmonia, proton-proton collisions, heavy-ion collisions, LHC

Název práce: Studium produkce charmonií v proton-protonových a těžko-iontových srážkách na LHC

Autor: Martin Krivoš

Ústav: Ústav částicové a jaderné fyziky

Vedoucí diplomové práce: doc. Mgr. Martin Spousta, Ph.D., Ústav částicové a jaderné fyziky

Abstrakt: V tejto práci sme sa zaoberali prote dukciou J/ψ mezónov v protón-protónových a ťažko-iontových zrážkach. Porovnali sme Monte Carlo generátor s datami z experimentu ATLAS, ktorý je súčasťou LHC. Za Monte Carlo generátor sme zvolili program PYTHIA, veriza 8.2. V prvej časti práce sme porovnali niekoľko rôznych nastavení PYTHI-e, na určenie najlepšej konfigurácie tak, aby sa čo najlepšie zhodovala s datami. Všetky naše zrážky boli uskutočnené pri ťažiskovej energii 7 TeV. Zistili sme, že výber partónových distribučných funkcií nemal viditeľný vplyv, no počiatočná a koncová radiácia partónov áno. V druhej časti sme korelovali tvorbu J/ψ s tvorbou jetov v eventoch. Jety boli zkonštruované anti-k_t jetovým algoritmom s polomerom $R = 0,4$. Na indetifikovanie J/ψ mezónov sme použili miónové páry. Zistili sme, že menej ako 10% J/ψ ide asociovať s jetmi.

Klíčová slova: charmonia, proton-protonové srážky, těžko-iontové srážky, LHC

Contents

Introduction

Collisions of heavy-ions at ultrarelavistic energies were shown to produce many interesting observations and could lead to better understanding of the very early universe just after the Big Bang. Quark-gluon plasma (QGP), the medium of quarks and gluons, was observed in these collisions. Presence of QGP is responsible for several new phenomena such as suppression of jets, called jet-quenching, charmonia suppression, or elliptic flow.

The structure of this thesis is as follows: The first chapter briefly summarizes general theoretical background of particle physics, namely the Standard Model and Quantium chromodynamics. This is followed by introducing the concept of jet and jet algorithms. In the second chapter, heavy-ion collisions are introduced. This chapter covers phenomena of jet quenching and charmonia suppression. Glauber model and important qunatity - Nuclear modification factor are also explained. The third chapter describes the Large Hadron Collider (LHC) at CERN and, in details, one of the four major expertiments of LHC - A Toroidal LHC ApparatuS (ATLAS). In the fourth chapter, the reader can get more detailed information about PYTHIA settings and ATLAS data samples used for the analysis. The fifth chapter, as the name implies, contains original results on charmonia and jet production. The last chapter closes with the discussion of the results and suggestions for further research.

Chapter 1

Strong interaction and proton-proton collisions

In the first chapter we will introduce theoretical background – the Standard Model of particle physics and Quantum chromodynamics, the theory of strong interactions.This is followed by the introduction to the concept of jet, parton distribution functions, and initial and final state radiation. At the end of this chapter we provide a brief summary of properties of charm quark.

1.1 The Standard Model

Standard model (SM) is theory of elementary particles describing three of the four known forces - electromagnetic, weak (or electroweak) and strong force [1]. It explains the fundamental properties of particles and their interactions in the framework of the quantum field theory. All particles are divided into two groups: massive particles (leptons and quarks) with spin 1/2 and massless particles - bosons with integer spin, which intermediate the interactions (see Figure 1.1). The SM was developed by theoretical and experimental physicists in the second half of the 20th century. The current formulation has been finalized in 1970s, while some particles were discovered much later namely the top quark (1995), the tau neutrino (2000), and the Higgs boson (2012).

Despite all the success, SM does not incorporate the gravitational force, which prevents it from being the unifying theory of all forces. Neutrino oscillations, dark matter and baryon asymmetry are examples of phenomena that are not explained within SM. The success of SM was a prediction of new particles which were later discovered. In particular gluons, Higgs boson, top quark and charm quark - whose discovery is described in Section 1.6.

For this thesis the most important part of the SM is Quantum chromodynamics (QCD) - a theory of strong interactions. The introduction to QCD is provided in the following Section 1.2.

1.2 Theory of Quantum Chromodynamics

QCD is theory of interaction of 'coloured' particles, namely quarks and gluons. Similarly to quantum electrodynamics (QED), QCD is a Yang-Mills theory, but

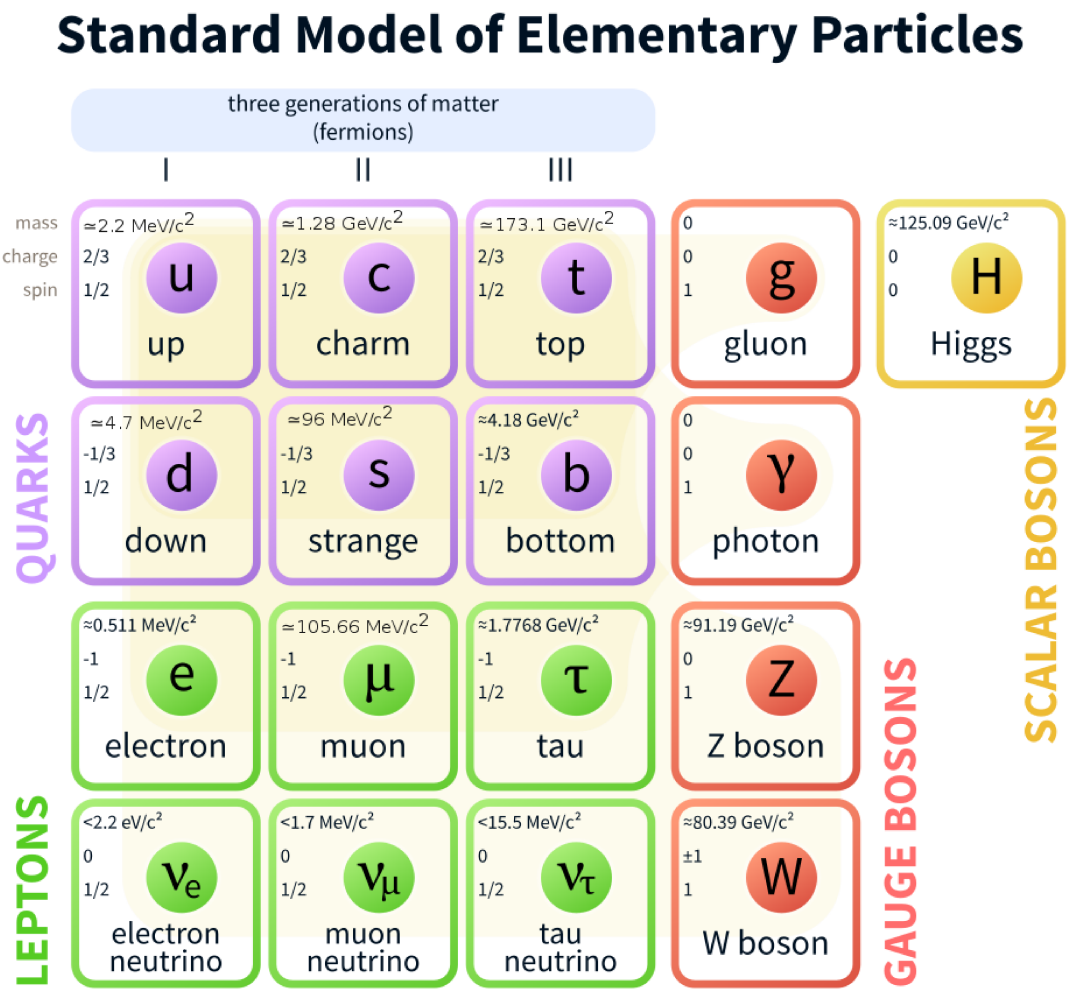

Figure 1.1: Table of all elementary particles forming the Standard Model. Picture taken from [2]

based on SU(3) non-Abelian symmetry group. As with any other Yang-Mills gauge fields, one requires local gauge invariance of the Lagrangian which reads

$$\mathscr{L}_{QCD} = -\frac{1}{4} F^C_{\mu\nu} F^{C\mu\nu} + \sum_f \bar{\psi}_f (i\gamma^\mu D_\mu - m_f)\psi_f, \tag{1.1}$$

where f is the flavour of the quarks with mass m_f, γ^μ are Diracs matrices, C is the colour index, running from 1 to 8 (which corresponds to dimensions of $SU(3)$ group), ψ_f is the Dirac spinor field of corresponding flavour f. D_μ is covariant derivative defined as

$$D_\mu = \partial_\mu - ig \sum_C t^C A^C_\mu, \tag{1.2}$$

where A^C_μ are gluon gauge fields and t_C are generators of the SU(3) group satisfying the Lie algebra commutation relations

$$[t_A, t_B] = i f_{ABC} t_C, \tag{1.3}$$

where f_{ABC} are structure constants of the SU(3) group. In matrix representation, these are 3x3 Gell-Mann matrices. The kinetic term is written in the form of

field strength tensors $F^C_{\mu\nu}$ (factor -1/4 in (1.1) is for consistency with the Maxwell equations) defined as:

$$F^A_{\mu\nu} = \partial_\mu A^A_\nu - \partial_\nu A^A_\mu - g f_{ABC} A^B_\mu A^C_\nu. \tag{1.4}$$

Local gauge transformation of half-spin quark fields reads as follows

$$\psi'_a(x) = e^{i\omega(x)}\psi_a(x) = U_{ab}\psi_b(x) \tag{1.5}$$

and gauge fields transform is

$$A'_\mu = A_\mu + \frac{i}{g}\partial_\mu \omega(x). \tag{1.6}$$

Relation between g and strong coupling constant α_s is

$$g = \sqrt{4\pi\alpha_s}. \tag{1.7}$$

This constant 'dictates' the strength of the interaction.

One can separate free and interaction part of the Lagrangian (1.1) and find out that there are exactly three possible interaction vertices. The interaction part then reads

$$\mathscr{L}_{int} = gA\bar{\psi}\psi + gAA\partial A + g^2 AAAA. \tag{1.8}$$

The first vertex is very familiar from QED. It connects the gluons, with massive quarks. While the abelian U(1) QED does not allow two gauge bosons (photons) to interact with each other, QCD has two vertices in which such interaction is possible. Therefore second and third term in (1.8) represent three and four gluon interaction, respectively. This difference is caused by the fact that gluons carry charge - colour charge, while their QED counterparts, photons, are neutral particles, and therefore cannot interact directly. Also note that two first terms are proportional to g lineary, while the last term is of order g^2 (see Figure 1.2 for corresponding Feynman diagrams).

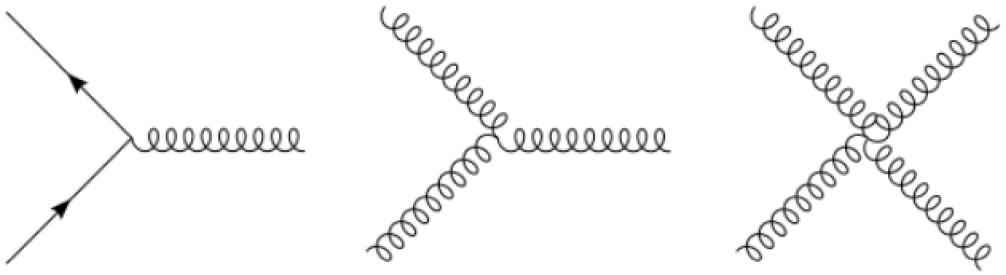

Figure 1.2: Three possible feynman diagrams of interaction vertices of QCD corresponding to interaction Lagrangian (1.8)

This non-abelian structure of QCD leads to two surprising phenomena, namely colour confinement and asymptotic freedom. Colour confinement is special feature of the strong interaction which ensures that all observable particles are colour singlets. Due to this, only hadrons and bosons are observable by detectors. Despite the 'lack of visibility' of quarks, their existence was proven by many experiments starting by the deep inelastic experiments [3]. Asymptotic freedom causes interactions between particles to become asymptotically weaker as the energy scale increases and the corresponding length scale decreases.

Running couplings

Using the perturbation expansion, one can find that QCD diverges for loop diagrams at large momenta - these divergences are cured by the procedure called renormalization. As SM itself, QCD is renormalizable theory. We will not carry out any detailed calculations nor will we introduce any theoretical background to the renormalisability of this theory. For more information see e.g. [4].

Renormalization introduces the renormalization scale μ. Renormalization scale dependence of α is controled by the beta-function and described by the *Renormalization group equation*:

$$\beta(\alpha_s) = \mu^2 \frac{\partial \alpha_s}{\partial \mu^2} = -\alpha_s^2(b_0 + \alpha_s b_1 + ...), \tag{1.9}$$

where b_0 and b_1 are constants and in case of mass-less quarks, they are independent of renormalization scheme:

$$b_0 = \frac{1}{12\pi}(11N_c - 2n_f), \tag{1.10}$$

$$b_1 = \frac{1}{24\pi^2}(17N_c^2 - 19n_f), \tag{1.11}$$

where n_f is the number of quark flavours and N_c is the number of colours. Terms b_2 and higher depend on the renormalization scheme and are beyond the scope of this thesis [5, 6, 7].

The equation of renormalization group (1.9) can be solved for one-loop

$$\alpha_s(\mu) = \frac{\alpha_s(\mu)}{1 + b_0 \alpha_s(\mu_0) \ln \frac{\mu^2}{\mu_0^2}} \tag{1.12}$$

and by some manipulation becomes:

$$\alpha_s(\mu) = \frac{1}{b_0 \ln \frac{\mu^2}{\Lambda_{QCD}^2}}, \tag{1.13}$$

where $\Lambda_{QCD} \approx 200 - 400$ MeV is the Landau pole where the coupling constant will be infinite at the leading order (LO) and perturbative calculations cannot be used.

Based on the sign of b_0, perturative quantum field theory can have Landau pole at either small μ or at very large one - See Figure 1.3. From (1.10) it is clear that b_0 is positive, therefore, QCD is asymptoticaly free.

Several measurements of the coupling constant α_s as a function of energy scale μ are show in Figure 1.4, along with the theoretical prediction of QCD. Usually, the value of α_s is explicitely calculated for $\mu = m_Z^2$ which is [5]

$$\alpha_s(m_Z^2) = 0.1181 \pm 0.0011. \tag{1.14}$$

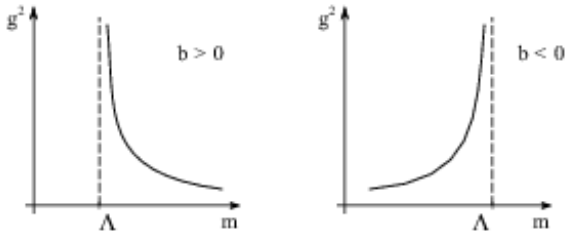

Figure 1.3: Two possibible types of Landau poles, based on the sign of b_0 constant. Here m on x-axis is renormalization scale.

1.3 Initial and final state QCD radiation

Initial and final state radiation are effects which take place before/after the main reaction. They influence the particles entering/leaving the process and therefore are unomittable part of the collision.

Final state radiation (FSR) describes emissions of partons from partons leaving the hard scattering interaction. Partons leaving hard process usually carry a high virtuality. This virtuality is reduced by FSR until it becames zero, eventualy. All radiated partons undergo hadronisation process (described in Section 1.4) to form observable hadrons.

Initial state radiation (ISR) describes emissions of partons from partons in hadrons which takes place before the hard scattering process.

In commonly used general purpose Monte-Carlo (MC) generators such as PYTHIA or HERWIG, ISR and FSR are modeled by parton showers and are subject of parameter tuning which allows to match the predictions of MC generators with the measured data. As will be demonstrated in Chapter 5, both ISR and FSR have big impact on the quantification of charmonia production.

1.4 Jets and hadronisation in QCD

As previously metioned, quarks cannot be observed as free particles (as a consequence of confinement). Suppose two protons colliding at high energies. During this process, fine structure of proton is visible to the process and quarks interact with each other. The energy of the strong field between quarks outgoing from the hard scattering increases with increasing distance between them. At some point this energy is large enough to create a new quark anti-quark pair form the vacuum. Such newly created particles recombine among themselves and with the original outgoing parton and form hadrons. This process is called *hadronisation* and is depicted in Figure 1.5.

These hadrons are usually collimated around the direction of primary parton and are either detected directly or by their decay products. By grouping these particles using some logic we can recreate kinematic properties of the original parton. Such group is called jet. Jet may contain particles of all types including hadrons, leptons or photons. Study of jet properties is of primary importance in hadronic collisions. QCD theory behind jets is far beyond the scope of this thesis. Next Section describes how to reconstruct jets from the data acquired by

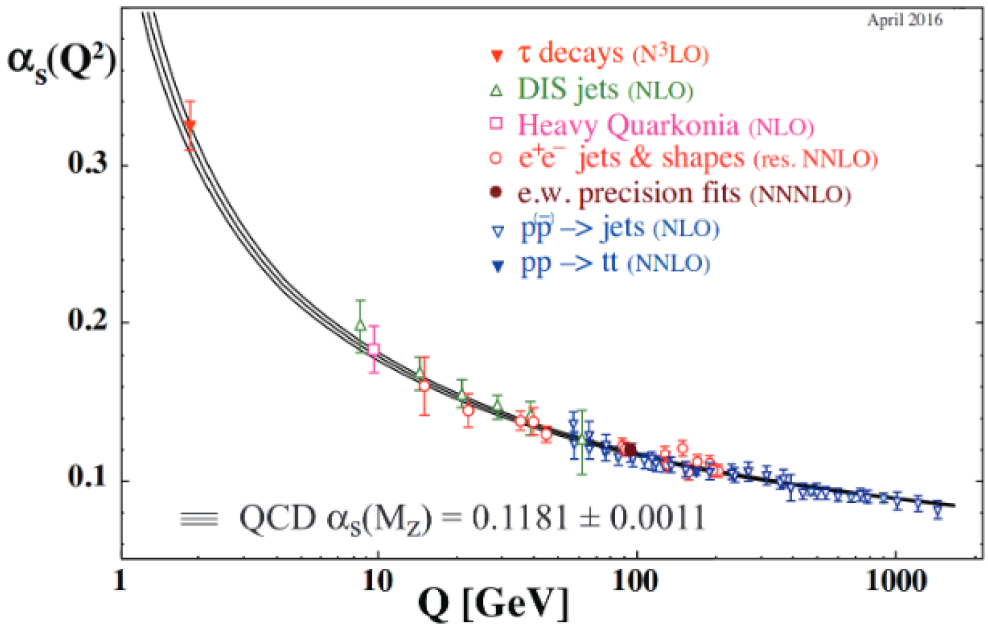

Figure 1.4: Different measurements of the running coupling α_s as a function of renormalization scale $\mu = Q$. Degree of perturbative theory is indicated in brackets, e. g. next-to-leading order (NLO), next-to-next-to-leading order (NNLO). Black lines represent theoretical prediction. Figure taken from [5].

the experiment.

1.5 Jet algorithms

Construction of jets is done by using some of the jet algorithms. It is important to note that no two jet algorithms are alike and the kinematic of jets between them will not perfectly match. We distinguish two main types of jet algorithms:

- Cone algorithms
- Sequential (or clustering) algorithms

Cone algorithms group particles that are close in the angle - are in the same cone. They encounter several difficulties, namely infrared and collinear (IRC) unsafety. Infrared unsafety is a case when a jet defined by the jet algorithm changes by adding one soft particle. Collinear unsafety is when jets change in a case e.g. by adding one soft particle between two jets. Jets must not change by adding soft gluon nor should be dependent on the order of the particles in which we process them. For this purpose sequantial algothitms were introduced as an improvement.

Sequantial jet algorithms

Each clusteing algorithm has two properties: It decides which particles are to be clustered together and when to terminate clustering, therefore leaving the final product.

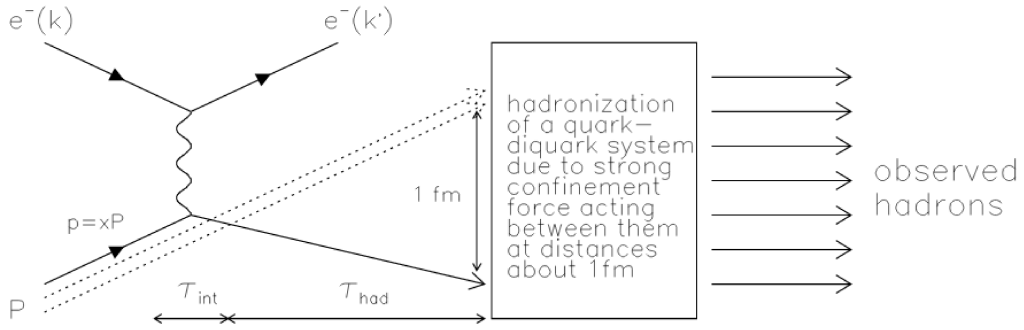

Figure 1.5: Scheme of hadronisation on example of electron-proton collision. Figure taken from [8].

The formula

$$\Delta R_{ij} = \sqrt{(y_i - y_j)^2 + (\phi_i + \phi_j)^2} \tag{1.15}$$

defines the space distance in $y \times \phi$ space between objects i and j, where y_i is rapidity of the i-th particle and ϕ_i is azimutal angle of the i-th particle (for definition of kinematic variables such as rapidity see Section 3.2.1). The algorithm defines two quantities d_{ij} and d_{iB}:

$$d_{ij} = min(p_{Ti}^{2k}, p_{Tj}^{2k})\Delta R_{ij}^2, \tag{1.16}$$

$$d_{iB} = p_{Ti}^{2k} R^2 \tag{1.17}$$

the later is reffered to as beam distance. R is a parameter which controls the size of the jet. In ATLAS experiment, $R = 0.4$ or $R = 0.6$ are typically used. The constant k determines type of the algorithm. $k = -1$ stands for so-called anti-k_t algorithm [9], $k = 1$ is for k_t algorithm [10, 11] and $k = 0$ is the Cambridge-Aachen algorithm [12] . The ATLAS expriment uses anti-k_t algorithm.

The sequence of the algorithm is as follows:

- Determine d_{ij} for all pairs of objects and do the same for the beam distance d_{iB}.
- Find i and j objects with minimum d_{ij} and d_{iB}.
- If $d_{ij} < d_{iB}$ combine i and j objects.
- If $d_{iB} < d_{ij}$ object i is final jet and is removed from the list.
- Repeat until the particle list is empty.

Both k_t and anti-k_t algorithms have their advantages and disadvantages which we will not discuss here. For an illustration we show one specific example, where different jet algorithms yield different results (Figure 1.6).

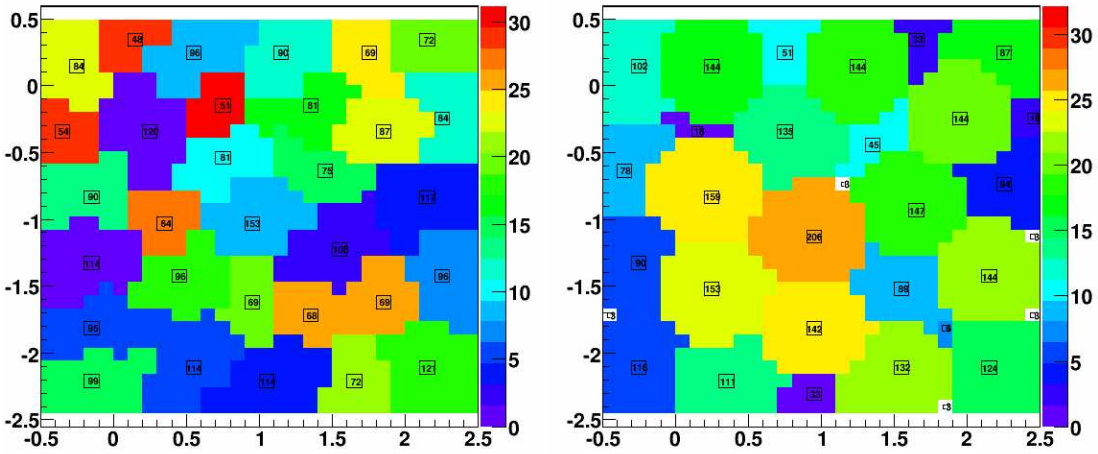

Figure 1.6: k_T (left) and $anti-k_T$ (right) algrithm on the same data sample [13].

1.6 Charmonia - a brief introduction

Quarkonia are bound states of quark and anti-quark of the same flavour. All quarkonia are therefore flovourless mesons. Although up, down and strange quarks do form quarkonia, the term is usually meant only for heavy quarks. Also top quarks and anti-quarks together are unable to form a bound state, as (anti)top quarks decay faster before a bound state can be created (a very rare case in which electroweak interaction preceeds strong interaction). Therefore only charm and bottom quark can create quarkonia which are called charmonia and bottomonia, respectively. Example of bottonium is *Upsilon* meson. Tho focus of this thesis is on the charmonia. In the next text, we will therefore describe their disovery and properties.

In 1970 theoretical physicists S. Glashow, J. Iliopoulos and L. Maiani added fourth quark as part of what is now as GIM mechanism [14] (at that time, only up, down and strange quarks were known and observed). This intension was to introduce aestheticaly pleasing lepton-quark symmetry $u, d, c, s \leftrightarrow e, \nu_e, \mu, , \nu_\mu$ (τ lepton family was not discovered yet). They named it charm quark, having spin 1/2 and holding charge of +2/3.

The very first discovered particle which constituent was a charm quark was J/ψ meson. Having rest mass of $m = 3096.916 \pm 0.011$ MeV and decay width $\Gamma = 92.9 \pm 2.8$ keV [5], it is today considered a ground state charmonium ($c\bar{c}$). It is the only particle to have two-letter name, as it was discovered simultaneously by two groups. The first exited state is denoted $\psi(2S)$ indicating its quantum state, with rest mass $m = 3686.109 \pm 0.014$ GeV and decay width $\Gamma = 304 \pm 9$ keV. In this thesis we will however focus mainly on the ground state. In this thesis only muonic decays were studied.

Chapter 2

Heavy-ion collisions

This chapter will provide a brief introduction to the physics of heavy-ion collisions and define basic terms such as quark-gluon plasma, jet quenching, Glauber model, and nuclear modification factor.

2.1 Quark-Gluon Plasma

For a few millionths of a second, shortly after the Big Bang, the universe was filled with particles of all types. This mixture was dominated by quarks and gluons. In those first moments of extreme temperatures, quarks and gluons were deconfined from hadrons and formed a state of matter which is called *quark-gluon plasma* and is recreated in heavy-ion collisions. This is in contrast with elementary collisions such as *pp* collisions where QGP does not appear. A basic illustration of the difference between *pp* and heavy-ion collisions is depicted in Figure 2.1 [15]. An

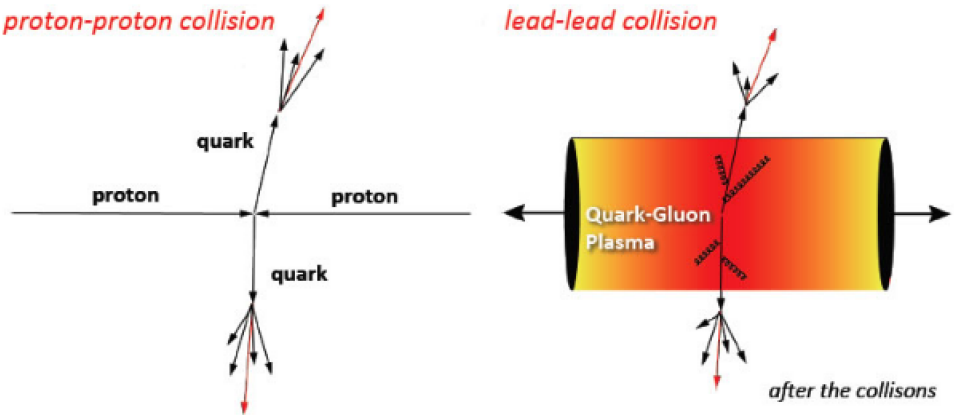

Figure 2.1: Cartoon showing the difference between simple *pp* collisions (to the left) and heavy-ion collision(to the right). QGP is present only in the right case, therefore hitting with ions is the only way to reproduce these conditions. Noticeable is the Lorentz contraction of nuclei in direction of the axis of the collision [16]

early discovery was that the quark-gluon plasma behaves more like a perfect fluid

with viscosity smaller than that of a gas. A theory of relativistic hydrodynamics is used to study some of the properties of QGP.

First ion collisions were performed at LBNL USA and JINR USSR with energy scales of $1 - 2$ GeV per nucleon. Later experiments are Alternating Gradient Synchrotron ($\sqrt{s_{NN}} \leq 5$ GeV), Super Proton Synchrotron ($\sqrt{s_{NN}} \leq 20$ GeV) at CERN, the Brookhaven Relativistic Heavy-Ion Collider ($\sqrt{s_{NN}} \leq 200$ GeV) and the Large Hadron Collider ($\sqrt{s_{NN}} \leq 5.5$ TeV) also at CERN.

A very convenient way to study the QGP is to use jets penetrating through the QGP. These jets undergo a process named *jet quenching* which is described in the following section.

2.2 Jet Quenching and charmonia suppression

The main method of studying QCD processes is studying yields and properties of jets created in e^-e^+, ep or hadron-hadron collisions. With ion collisions it is no different. As mentioned above, QGP is created in the interaction. This QGP heavily affects the properties of jets. These effects are called *jet quenching*.

Bjorken suggested [17] that if two partons travel a different path length in the medium, back-to-back jets would be sensitive to differential energy loss of partons propagating through QGP. The loss may be so severe that the entire jet is absorbed. Bjorken estimated energy loss per path length, dE/dx, based on the elastic collisions of partons of high momentum with QGP constituents (resulting relation reminds one of ionisation energy loss):

$$\frac{dE}{dx} = C_R \pi g^2 T^2 (1 + \frac{N_f}{6}) \ln \frac{4ET}{m_D^2}, \tag{2.1}$$

where C_R is the colour factor (3 for gluons and 4/3 for quarks). T is plasma temperature, N_f is the number of quarks flavours, g is the coupling parameter and m_D is Debye screening mass, defined as:

$$m_D = (1 + \frac{N_f}{6}) g^2 T^2. \tag{2.2}$$

On top of that, partons lose energy via gluon radiation or so called gluon-strahlung (a QCD analogy of bremstrahlung). As the parton travels through the medium, it radiates gluons which interact with the medium and effectively becomes a part of it. A sketch of the jet quenching is in Figure 2.2 while in the Figure 2.3 real example of the event display with quenched jets recorded by ATLAS is shown.

Not only jets but also charmonia can be used as tools to reveal the properties of the medium and its interactions. The production of charmonia in elementary collisions is often described in a nonrelativistic QCD effective-field-theory (EFT) framework [18]. In that theory, first, the $c\bar{c}$ pair is produced either in a color singlet or color octet state. This "pre-resonant" $c\bar{c}$ pair then binds into a physical charmonium by non-perturbative evolution described in terms of long-distance matrix elements. The pre-resonant pair in the color octetstate changes its color and spin by radiating off gluon(s) when evolving to the physical quarkonium state while the pair in the color singlet state retains these quantum numbers unchanged

[19]. When charmonium or the pre-resonant $c\bar{c}$ pair propagates through the QGP, the Debye screening may lead to weakening of the interaction between c and $\bar{c}$ quark leading to the disintegration of charmonia. This can be observed as a suppression of the charmonia production.

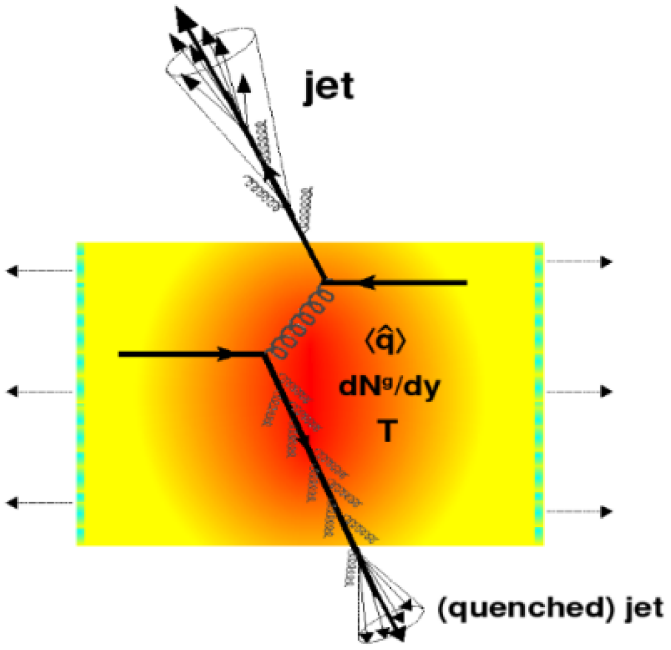

Figure 2.2: Sketch of an example of a quenched jet.

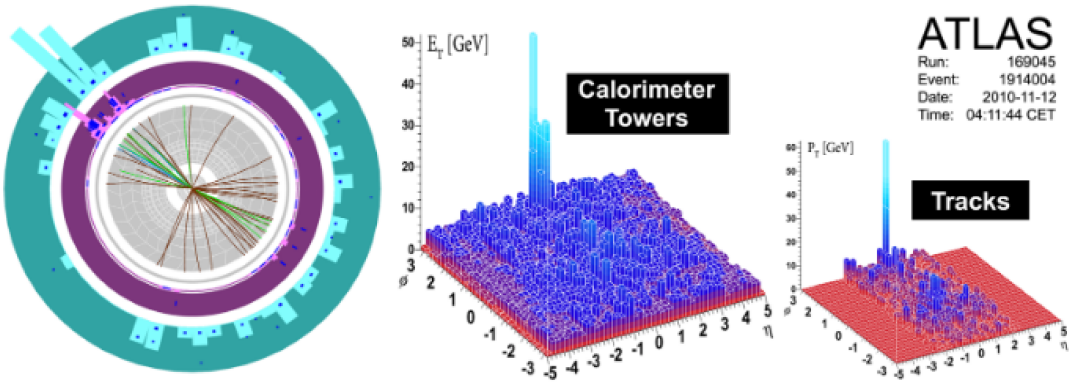

Figure 2.3: Event measured by ATLAS showing big suppression of one jet. Due to jet quenching, only one jet is present [20].

2.3 Glauber model

Experiment shows that in the heavy-ion collisions a large multliplicities of charged particles are generated. During this collision two Lorentz contracted nuclei collide at impact parameter b in their centre-of-mass reference frame. Impact parameter

b, is the transverse distance of the centers of the nuclei. See scheme in Figure 2.4. If the impact parameter is large, peripheral collision occurs. In this case one observes low multiplicities and collisions are very simlar to simple proton-proton collisions. On the contrary if the impact factor is low and the overlap of the two nuclei is large, large multiplicities are observed.

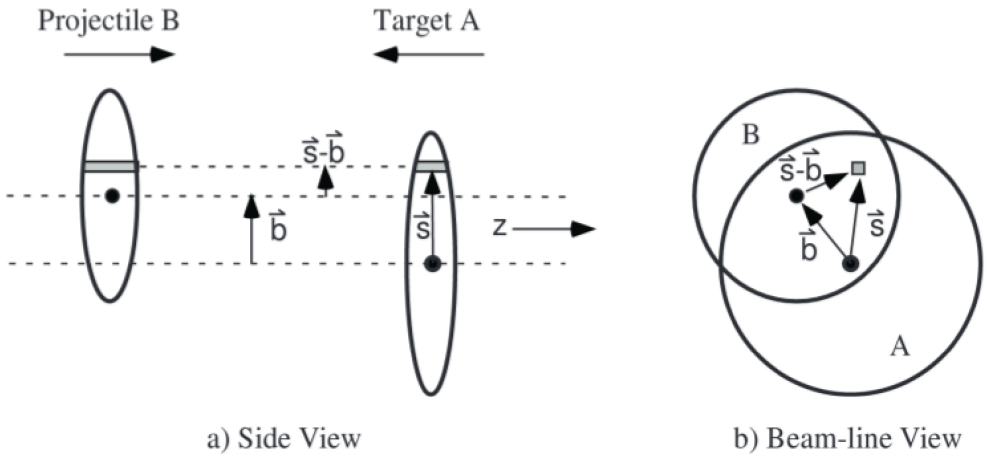

Figure 2.4: Shematic view of two Lorentz contracted discs colliding at impact parameter b. A view from a side, parallel to the beam-line (let) and front side perpendicular to the beam-line (right) is shown [21].

A basic model can be used to describe these collisions using phenemonological approach. This model is called *Glauber model* [21, 22]. Glauber model assumes superposition of all nucleon-nucleon interactions. The reaction is composed of a sequence of independent collisions and all nucleons travel in the direction of the beam-axis (all transverse movement is neglected and collisions are smoothly distributed). A Woods-Saxon distribution [23] describes the nuclear density ρ at a distance r from the centre of the nucleus:

$$\rho(r) = \frac{\rho_0}{1 + e^{(r-R)/a}}, \tag{2.3}$$

where R is radius of the described nucleus of N nucleons ($R = R_0 N^{1/3}$ is used, where $R_0 = 1.18$fm) and a is the skin thickness. Constant ρ_0 ensures normalization of the distribution to the number of nucleons.

A key quantity in Glauber model is the nuclear thickness function $T_A(s)$ which is defined as

$$T_A(s) = \int \rho_A(s, z) dz, \tag{2.4}$$

where s is a transverse distance of the nucleon A from the centre of its nucleus. $T_A(s)$ has a meaning of number of nucleons in unit area along a direction of z-axis.

To calculate the interaction probability of colliding nucleons which are inside the two nuclei, one can introduce the normalisation overlap function

$$T_{AB}(b) = \int T_A(s) T_B(s - b) ds, \tag{2.5}$$

where b is the impact parameter. The probability of one inelastic nucleon-nucleon collision is then $T_{AB}(b)\sigma^{NN}$ where σ^{NN} is the nucleon-nucleon inelastic cross-section.

The probability of n inelastic collisions with an impact parameter b is

$$P(n,b) = ABn[T_{AB}(b)\sigma^{NN}]^n[1 - T_{AB}(b)\sigma^{NN}]^{AB-n} \tag{2.6}$$

and total probability is defined as

$$\frac{d\sigma^{A+B}}{db} = \sum_{n=1}^{AB} P(n,b) - 1 - [1 - T_{AB}(b)\sigma^{NN}]^{AB}. \tag{2.7}$$

Now average number of binary collisions N_{coll} can be calculated:

$$N_{coll}(b) = \sum_{n=1}^{AB} nP(n,b) = ABT_{AB}(b)\sigma^{NN}. \tag{2.8}$$

Besides N_{coll}, one can calculate the number of participants, N_{part}, which is the number of nucleons that undergo an inelastic scattering in the collision. It is defined as:

$$N_{part}(b) = A\int T_A(s)\Big[1 - [1 - T_B(s-b)\sigma^{NN}]^B\Big]d^2s + B\int T_B(s-b)\Big[1 - [1 - T_A(s)\sigma^{NN}]^A\Big]d^2s.$$

Finally, nuclear overlap function can also be expressed in terms of σ^{NN} and average number of nucleon-nuclen collisions N_{coll} as

$$T_{AA} = \frac{N_{avr}}{\sigma^{NN}}. \tag{2.9}$$

2.4 Nuclear modification factor

Centrality of the lead-lead collisions have big impact on the yield of hadrons. Consequently, one needs to quantify the jet quenching as a function of collision centrality. The centrality of Pb+Pb collisions can be characterized by the sum of the transverse energy measured in forward calorimeters (E_T^{fwd}). The centrality describes the degree of geometric overlap of two colliding nuclei in the plane perpendicular to the beam with large overlap in central collisions and small overlap in peripheral collisions. Centrality intervals are defined in successive percentiles of the E_T^{fwd} distribution ordered from the most central (highest E_T^{fwd}) to the most peripheral collisions [24]. It was observed, that at fixed p_T jets lose approximately same amount of energy when passing though the QGP medium. The larger the E_T^{fwd} is, the larger is overlap of the two nuclei which leads to larger nucleon-nucleon luminosity. Nuclear overlap function T_{AA} is used to normalize yields. To quantify the magnitude of the suppression, we define *nuclear modification factor* R_{AA}

$$R_{AA} = \frac{\frac{1}{N_{evt}T_{AA}}\frac{d^2N}{dp_Tdy}\Big|_{cent}}{\frac{d^2\sigma_{pp}}{dp_Tdy}\Big|_{pp}}, \tag{2.10}$$

where N_{evt} is the number of heavy-ion collisions, d^2N/dp_Tdy is the differential yield for the jet production in heavy-ion collisions of a given centrality, $d^2\sigma_{jet}/dp_Tdy$ is the differential cross-section for the jet production in proton-proton collisions. When no jet quenching is present, nuclear modification factor is unity.

Another quantity which can characterize the magnitude of the jet suppressionis *central-to-peripheral nuclear modification* R_{CP} which is defined as

$$R_{CP} = \frac{T_{AA}|_{perip}\,(1/N_{evt}d^2N_{jet}/dp_Tdy)|_{cent}}{T_{AA}|_{cent}\,(1/N_{evt}d^2N_{jet}/dp_Tdy)|_{perip}}, \tag{2.11}$$

where $1/N_{evt}d^2N_{jet}/dp_Tdy$ is differential per event yield in hevy-ion collisions. $T_{AA}|_{cent}$ is nuclear overlap function for central events and $T_{AA}|_{perip}$ is nuclear overlap function, but for peripheral events. R_{CP} has a disadvantage which is weaking of the signal in the case that peripheral collisions are also suppressed. It is used only if the *pp* reference is not available.

Chapter 3

Experimental setup

In the first section of this chapter, Large Hadron Collider (LHC) at European Organization for Nuclear Research (CERN) in Geneva, Switzerland is be briefly introduced. Next, we decribe one of its main four detectors in detail - A Toroidal LHC ApparatuS (ATLAS). Other major experiments a Compact Muon Solenoid (CMS), A Large Ion Collider Experiment (ALICE) and Large Hadron Collider beauty (LHCb) will not be described here, although they also participate in the heavy-ion physics program of LHC. [1]

3.1 The Large Hadron Collider

The LHC is a sychrotron at CERN near Geneva, Switzerland. It was built in underground tunnel prieviously used for Large Electron-Positron Collider (LEP) and most of the time it runs pp collisions. Basic motivation to build LHC was the discovery of Higgs boson, the last piece of puzzle in the Standard Model. It was calculated that if Higgs bosons exists, the LHC would produce several particles per minute. In addition to that, the kinematic regime of LHC enabled to study hypothetical new particles such as particles of supersymmetry or W' and Z' bosons. Besides these discovery goals, LHC was intended to perform precision measurements of known SM particles and interactions. From its first run, LHC was several times upgraded. While at its first days its collison energy per proton was 450 GeV, today it operates at 6.5 TeV per proton. Since November 2010, LHC is regularly running also collisions of heavy-ions besides the standard pp collisions. In addition to lead, a short run with Xe beams colliding at the centre-of-mass energy of 5.44 TeV took place in autumn of 2018 LHC collides lead ions or proton and lead for a duration of one month in a year.

From technical point of view, LHC is currently the largest single machine in the world and the most powerful particle accelerator ever built. The main tunnel has 26. 7 km in circumference and lies 45 to 170 m below ground level and spans under Switzerland and France as well (Figure 3.1). The main circle is divided into four straight parts (where the main detectors are situated) and four curved parts. Inside, two parallel counter-rotating rings are used to speed-up the accelerated particles which intersect inside the detectors. Superconducting electromagnets with magnetic field of 8 Tesla are used to keep particles on their

[1] If not stated otherwise, all information and Figures in this chapter are taken from [25, 26, 27]

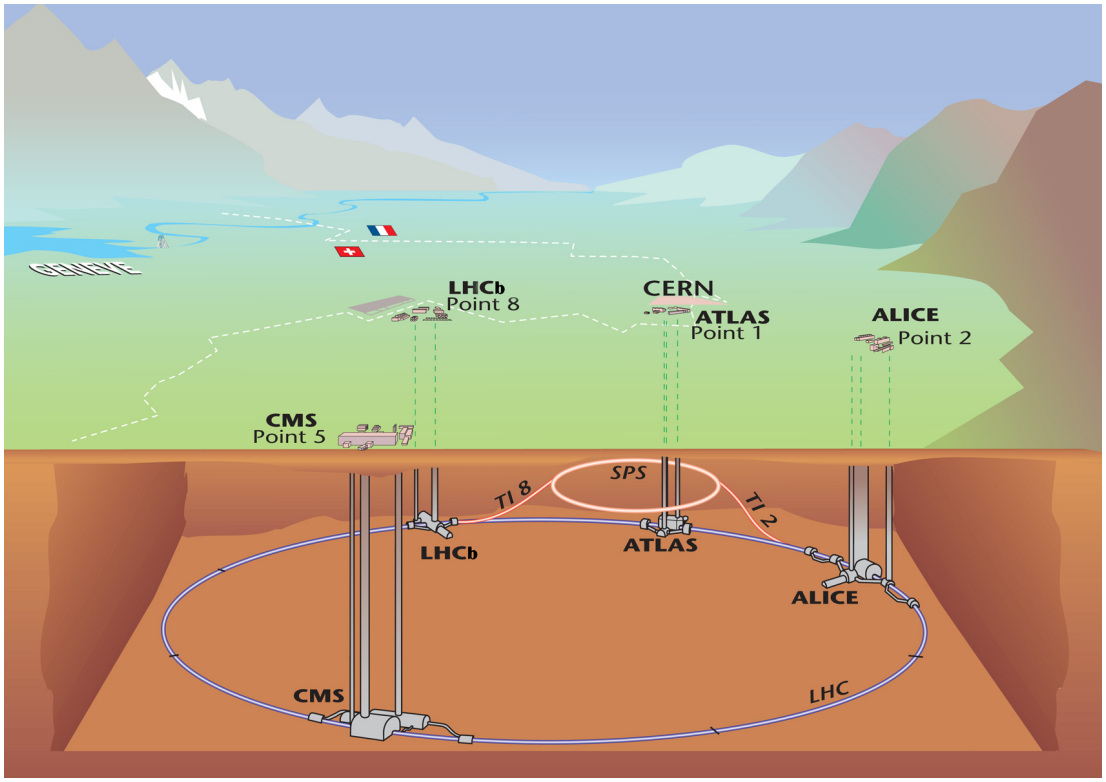

Figure 3.1: Scheme of LHC and its four major experiments underneath the Swiss-French border.

intended trajectory.

In addition to the main tunnel, there are several smaller accelerators, so called injectors, whose purpose is to inject protons or ions to the primary circuit. For protons the chain is Linac 2, the PS Booster (PSB), the Proton Synchrotron (PS) and the Super Proton Synchrotron (SPS) and for the ions it is Linac 3, the Low Energy Ion Ring (LEIR), the PS and the SPS [28]. The Pb 27+ ions extracted from the source must be fully stripped of all the electrons, before their injections to the LHC. For this purpose, the aluminium foil strippers are installed, the first one in Linac3 and the other between PS and SPS. See Figure 3.2.

In November 2010 an observation of a strong jet quenching at the LHC was announced [20]. In July 2012, the discovery of a new particle with a mass between 125 and 127 GeV was announced which was later confirmed to be the Higgs boson. [29, 30].

Luminosity is important quantity when describing a particle accelerator. To increase the chances of collision, particles travel in bundles. If two beams contain n_1 and n_2 particles in each bundle colliding with frequency f (number of collisions per second), *instantaneous luminosity* $\mathscr{L}$ is

$$\mathscr{L} = f\frac{n_1 n_2}{4\pi\sigma_x\sigma_y}, \tag{3.1}$$

where σ_x and σ_y are transverse beam profiles in x and y directions, respectively. We assume, that transverse profiles are identical and profiles are independent of the position along the bundle.

Along instantaneous luminosity, we define *integrated luminosity* which is sim-

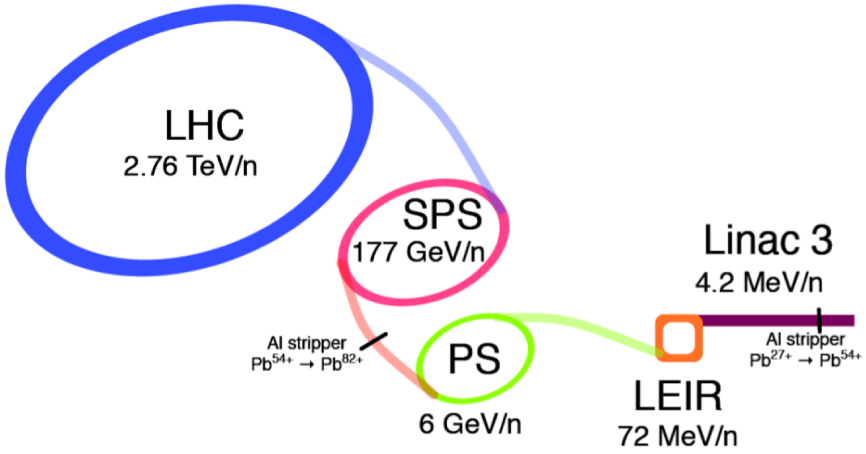

Figure 3.2: Scheme of LHCs heavy-ion injectors.

ply integral of $\mathscr{L}$ over time. Number of events N is then

$$N = \sigma \int \mathscr{L} dt, \tag{3.2}$$

where σ is the cross-section of the process.

3.2 The ATLAS experiment

ATLAS (A Toroidal LHC ApparatuS) is one of the four major experiments at the LHC (see Figure 3.3). It is located at interaction point 1 (IP1) of the LHC ring and is capable of detecting both proton-proton and heavy-ions collisions at unprecedented luminosity. It is also one of two general purpose detectors (along with Compact Muon Solenoid (CMS) Detector). Weighting over 7000 tons and cylindrical in shape, being 6 meters long and having a diameter of 25 meters it is the largest volume detector ever constructed for a particle collider. With its axial symmetry, the detector covers almost whole 2π azimuth angle.

The inner most part, *the Inner Detector* (ID), is the first part of the detector the colliding particles interact with. Its main purpose is to measure trajectories and transverse momenta of charged particles. It is placed in 2 Tesla solenoid magnetic field. After the ID, particles interact with the *Calorimeter*, measuring energies of strongly and electrmagnetically interacting particles. The last stage is *Muonic Spectrometer*, which allows to measures momenta of muons. All these parts are described in more details below.

Processing system is not directly embodied inside the detector, but plays an important role in the analysis of events, therefore a basic description is included at the end of this section.

3.2.1 ATLAS coordinate system

The origin of the ATLAS coordinate system is located in the nominal interaction point. The x-axis points horizontaly to the middle of LHC circle, y-axis points upwards and z-axis is parallel to the beam travel and its direction is so,

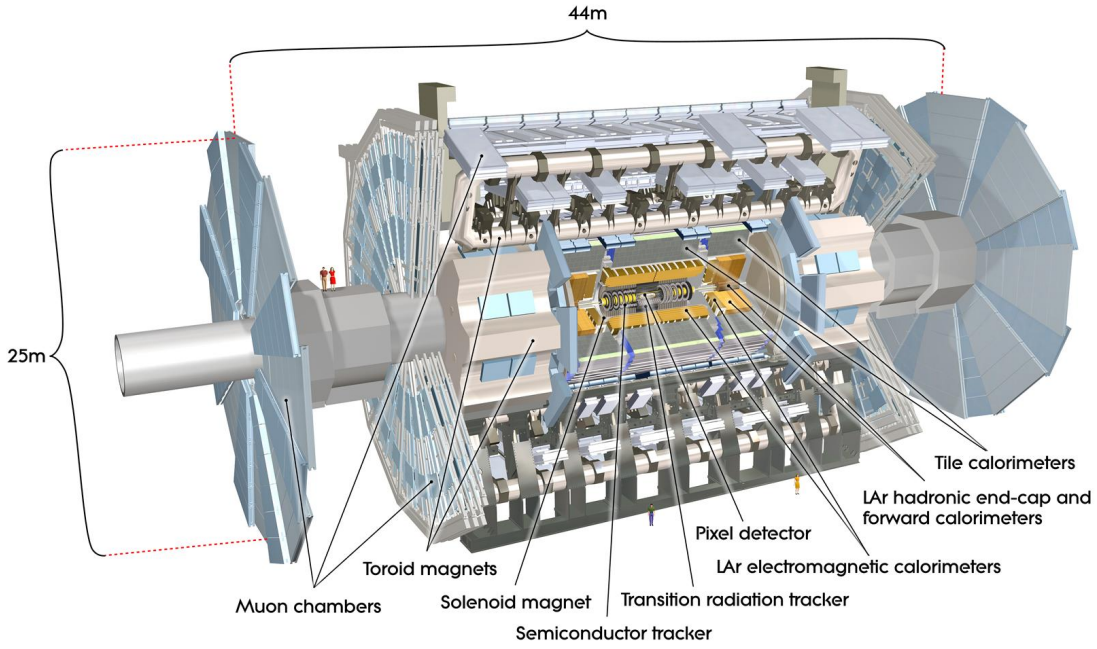

Figure 3.3: Cutaway view of the ATLAS experiment with human figures as a reference.

to create righ-handed system of coordinates. The detector is axially symmetric with respect to the z-axis. This symmetry naturaly prefers cylindrical coordinates (r, ϕ, θ). With r being the transverse radius from the z-axis, ϕ is the azimuthal angle in the $x - y$ plane and θ is the polar angle measured from the positive z-axis.

Rapidity which is, unlike velocity, additive in boosts, can be defined using four-vector $P = (E, p_x, p_y, p_z)$ as follows

$$y = \frac{1}{2} \ln \frac{E + p_z}{E - p_z}. \tag{3.3}$$

In our case, boost operates only along the z-axis (thus the formula (3.3) is rather simple). In the case of massless particles or for $m/|p| \to 0$, rapidity asymptotes to pseudorapidity which is defined as

$$\eta = -\ln\left(\mathrm{tg}\frac{\theta}{2}\right). \tag{3.4}$$

Pseudrapidity is not a function of mass and only polar angle is required.

Assuming two particles with momenta $p_1 = (E_1, \vec{p_1})$ and $p_2 = (E_2, \vec{p_2})$ collide, their centre-of-mass energy is:

$$\sqrt{s} = \sqrt{p_1^2 + p_2^2} = \sqrt{(E_1 + E_2)^2 - (\vec{p_1} + \vec{p_2})^2}, \tag{3.5}$$

which is a Lorentz invariant quantity.

During the acceleration of heavy-ions, only protons are accelerated, as neutrons are electrically neutral. Therefore what is known as nucleon-nucleon collision energy $\sqrt{S_{NN}}$ is introduced. Consider having proton accelerator, accelerating

the proton up to the energy E_p, then if ions with Z protons and A nucleons are used instead, nucleon-nucleon energy is

$$\sqrt{s_{NN}} = 2E_p \frac{Z}{A}. \tag{3.6}$$

3.2.2 ATLAS sub-detectors

As stated above, ATLAS consists of four major parts, all of which will be described here.

The Inner Detector

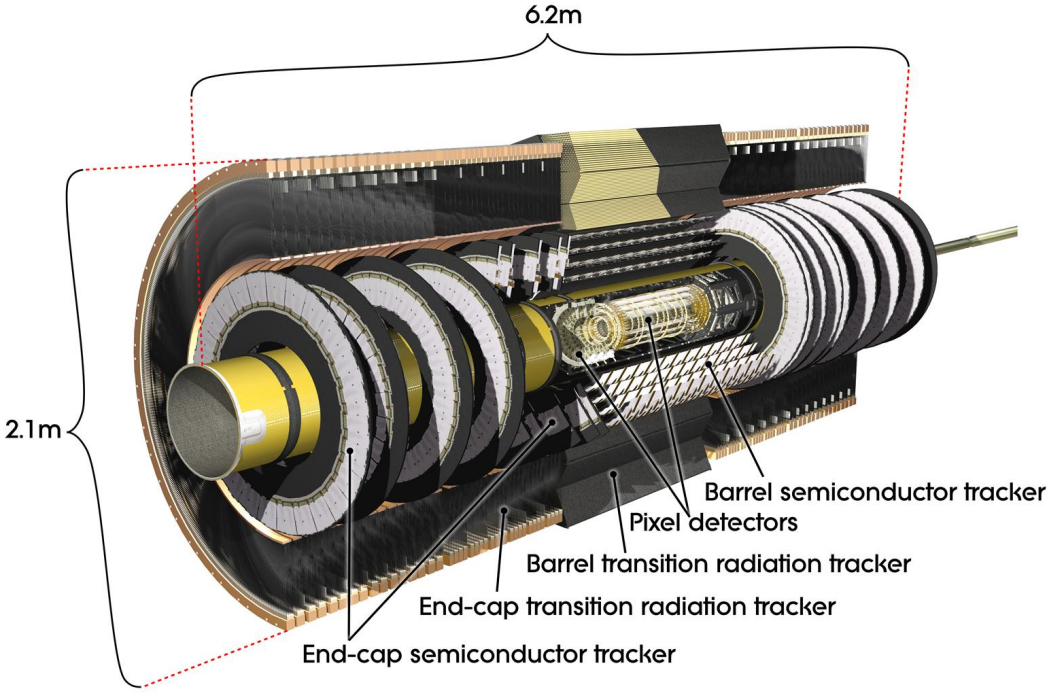

Figure 3.4: Cutaway of the Inner detector.

The Inner Detector (ID) is the first part of ATLAS which detects the particles produced in the collision. It measures direction, momentum and charge of electrically-charged particles. As mentioned previously, it is immersed inside 2 Tesla magnetic field which allows momentum measurements. The ID covers an angle up to pseudorapidity of $|\eta| = 2.5$. See Figures 3.4 and 3.5.

The inner-most part of ID is called *the Pixel detector* which consists of over 80 milion pixel detectors divided into three parts. A middle part is *Semiconductor tracker* (SCT) consisting of four barrels. It provides additional data for trajectory reconstruction. The last part, *the Transition Radiation Tracker* (TRT), provides particle identification and additional coordinates, using over 300 000 gaseous straws within 73 layers. The reason gas was used, was to minimize overal material needed to produce the ID.

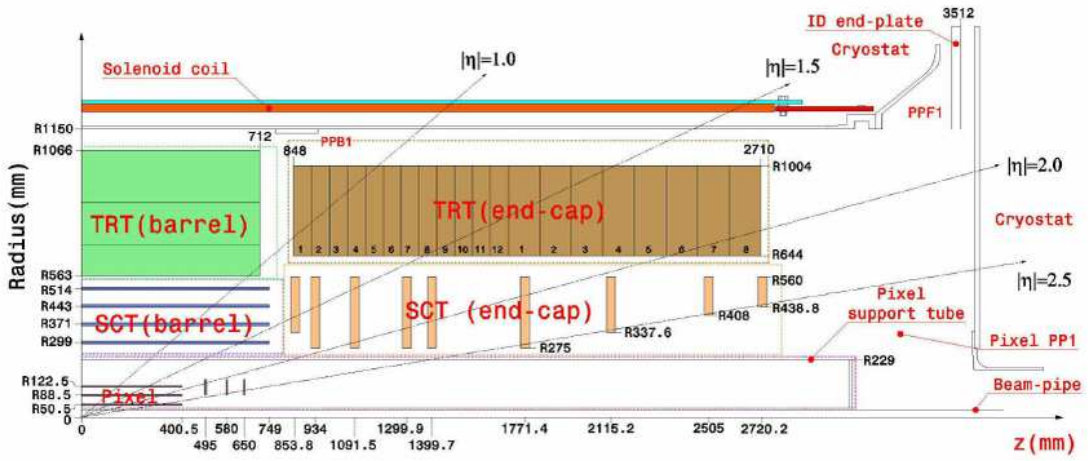

Figure 3.5: Schematics of the ATLAS Inner detector.

Calorimeter

Calorimeter is a type of detector which measures the energy loss of a particle as it passes through it. It does so by either stopping the particle entirely or absorbing a part of its energy. This way all the energy is transferred to the detector. For this purpose, highly absorbing materials are used and built in layers. For instace lead interleaved with layers of an "active" medium such as solid lead-glass or liquid argon. An basic layout of the ATLAS calorimeter is in Figure 3.6.

One can distinguish two main types of calorimeters, based on particles they absorb (and interactions via which they interact): electromagnetic and hadronic calorimeters.

Following this distinction, ATLAS calorimeters can be divided into two parts (See Figure 3.7):

- Liquid Argon (LAr) electromagnetic calorimeter
- Tile hadronic calorimeter.

Electromagnetic calorimeters measure the energy of electrons and photons as they interact with matter, while hadronic calorimeters sample the energy of hadrons as they interact with atomic nuclei. Calorimeters can stop most known particles except muons and neutrinos.

Muon Spectrometer

While most of the known particles are stopped in the calorimeter, muons are not. For this purpose, the outer-most layer of the ATLAS experiment, is the Muon Spectrometer. It consists of 4000 chambers in order to identify muons and their momenta. It has four main parts (Figure 3.8):

- Thin Gap Chambers - for triggering and second coordinate measurement (non-bending direction) at ends of the detector.
- Resistive Plate Chambers - for triggering and second coordinate measurement in the central region.

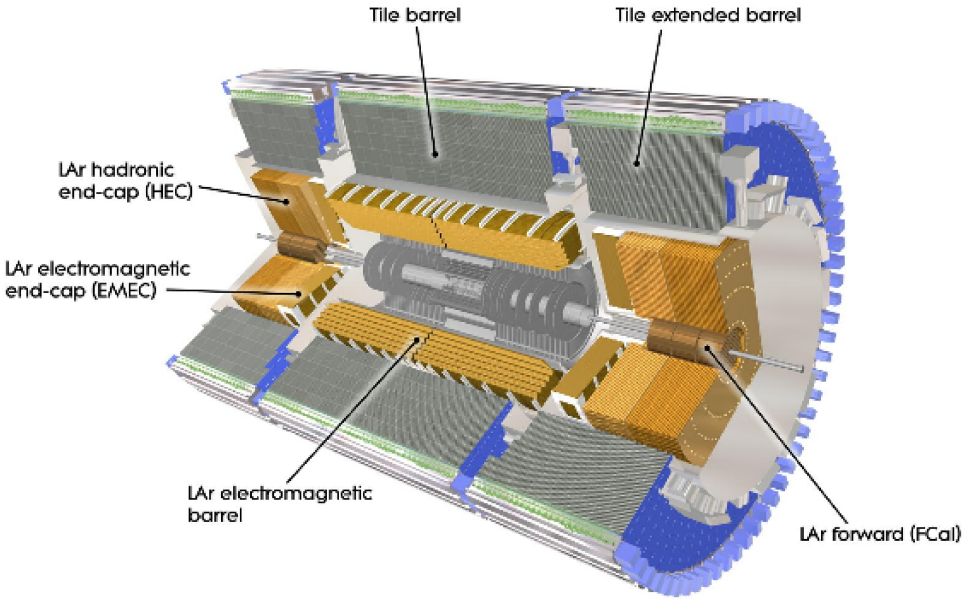

Figure 3.6: Cutaway of the ATLAS calorimeter

- Monitored Drift Tubes - measure curvature of tracks.
- Cathode Strip Chambers - measure precision coordinates at ends of the detector with the resolution of 60 μm.

Magnet System

Magnetic field is used to curve the trajectories of the charged particles for identification of their momenta and charges. It consists of three parts, namely Barrel Toroid (4 Tesla), End-cap Toroid (2 Tesla) and Central Solenoid Magnet (4 Tesla) - see Figure 3.9.

Triggers

The ATLAS experiment can observe up to billion proton-proton collisions per second. However, most of them are not of our interest for further processing. Trigger system selects only 100 events, out of this billion. In the case of the first running period of the LHC this was done in the following three stages

- The Level-1 trigger works on a subset of information from the calorimeter and muon detectors. The decision to keep the data from an event is made less than two microseconds after the event occurs.
- The Level-2 trigger is a large array of custom processors that analyse in greater detail specific regions of interest identified by the Level-1 system for each event.

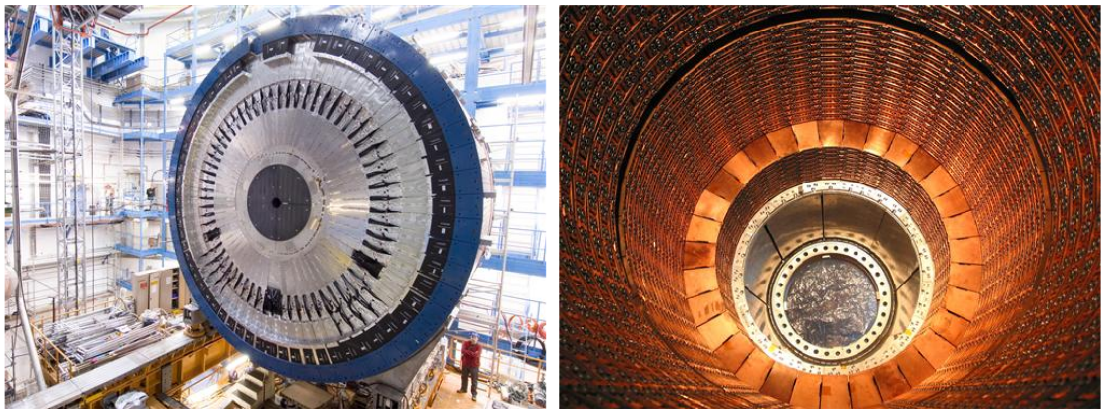

Figure 3.7: Picture of the ATLAS electromagnetic Calorimeter (left) and hadron calorimeter (right).

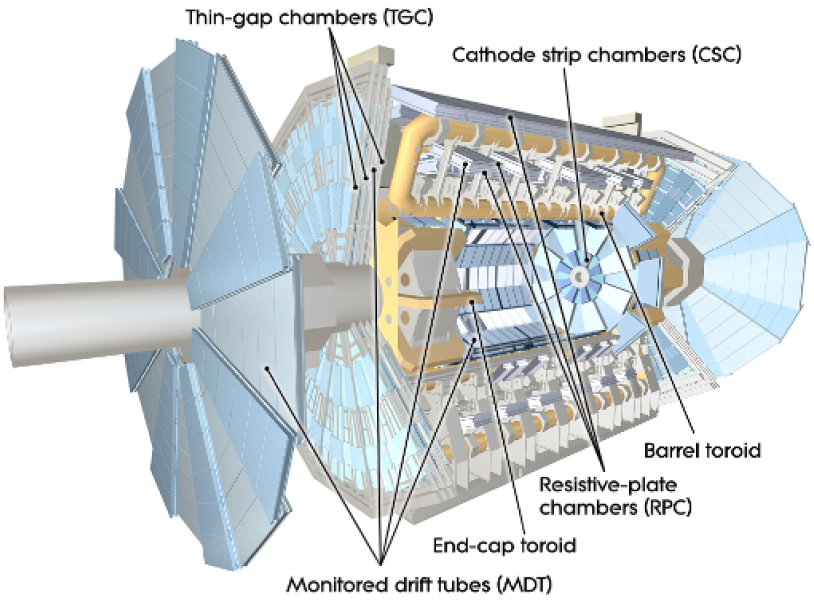

Figure 3.8: Cutaway of the ATLAS muon spectrometer

- The Level-3 trigger is a large farm of CPUs which perform a detailed analysis of the full event data.

In the second running period of the LHC (run 2), the trigger was rebuilt and Level-2 and Level-3 were joined into the High Level Trigger (HLT) which can run over both the regions of interest and the entire event.

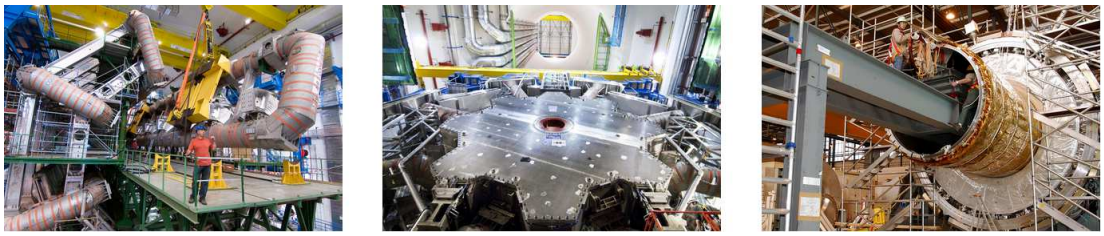

Figure 3.9: The ATLAS Magnet System.

Chapter 4

Data and MC samples

In this Chapter we will discuss the data and MC samples used in this thesis. First, we will describe the Monte Carlo generator (MC) that was used and its settings which we have used. At the end of this chapter we describe data samples and event selection that were used in the analysis of data collected by the ATLAS experiment.

4.1 PYTHIA MC generator

PYTHIA MC generator [31], version 8.235 was used in this study. PYTHIA is a standard tool for the generation of events of high-energy collisions of protons, pions or charged leptons, comprising a coherent set of physics models for the evolution from a few-body hard process to a complex multiparticle final state. It contains a library of hard processes, models for initial- and final-state parton showers, matching and merging methods between hard processes and parton showers, multiparton interactions, beam remnants, string fragmentation and particle decays. PYTHIA 8. 2 is the second main release after the complete rewrite from Fortran to C++, and now it has reached such a maturity that it offers a complete replacement for most applications, notably for LHC physics studies. The many new features should allow an improved description of data.

4.2 PYTHIA samples

In this section, we outline basic information about the PYTHIA settings. All the information is contained in the following code (for those unfamiliar with the syntax of PYTHIA, refer to the comments bellow or PYTHIA documentation).

```
Beams:eCM = 7000.
Main:numberOfEvents = 1000000
Main:timesAllowErrors = 10
Random:setSeed = on
Init:showAllSettings = off
Init:showChangedParticleData = on
Init:showAllParticleData = off

! common ATLAS Pythia8
Main:timesAllowErrors = 500
6:m0 = 172. 5
```

```
23:m0 = 91.1876
23:mWidth = 2.4952
24:m0 = 80.399
24:mWidth = 2.085
StandardModel:sin2thetaW = 0.23113
StandardModel:sin2thetaWbar = 0.23146
ParticleDecays:limitTau0 = on
ParticleDecays:tau0Max = 10.0

Tune:pp = 5

PDF:pSet=LHAPDF6:CT10nlo

!Charmonia common
!Hard process
PhaseSpace:pTHatMin = 5.      ! //# Equivalent of CKIN3
ParticleDecays:mixB = off

! Quarkonia production mode
Charmonium:all = on
PhaseSpace:pTHatMinDiverge = 0.5
! standard resonances decaying to J/Psi
445:onMode = off     ! // chi_2c
445:onIfAny = 443    ! // chi_2c
10441:onMode = off   ! // eta_c(2S)
10441:onIfAny = 443 !// eta_c(2S)
10443:onMode = off !// h_1c
10443:onIfAny = 443 !
20443:onMode = off   ! // chi_1c
20443:onIfAny = 443 !
! color triplet resonances decaying to J/Psi
9940103:onMode = off
9940103:onIfAny = 100443
9941103:onMode = off
9941103:onIfAny = 100443
9942103:onMode = off
9942103:onIfAny = 100443
! color triplet resonances decaying to Psi(2) [note: no color
    singlet resonances going to Psi(2)]
9940003:onMode = off
9940003:onIfAny = 443
9941003:onMode = off
9941003:onIfAny = 443
9942003:onMode = off
9942003:onIfAny = 443
! signal
443:onMode = off      ! // J/Psi
443:onIfAny = 13
100443:onMode = off   ! // Psi(2S)
100443:onIfAny = 13
```

On the first line we set centre-of-mass energy to 7 TeV, with default PYTHIA settigs of proton-proton collision. Centre-of-mass energy of 7 TeV was used for a comparison with published measurement of J/Psi production [32] discussed in Section 5.2. For a comparison of MC with data collected by ATLAS, centre-of-mass energy of 5.02 TeV was used. On the second line we specify number of events, as in this case it was one million. All events have random initial conditions

using basic PYTHIA pseudo-random generator. Line number 23 specifies PDF set we are using. In this particular case it is CT10nlo, but other PDFs were used too. As a default setting, PYTHIA has both ISR and FSR turned on. To switch them off, one has to add `PartonLevel:ISR = off PartonLevel:FSR = off` below line 23, respectively. The quarkonium production specified in lines 34-60 was chosen based on ATLAS settings [33].

Jets used in the MC have been reconstructed using anti-k_t algorithm with $R = 0.4$ implemented in the FastJet package. All stable particles, as defined by PYTHIA, except for muons and neutrina were used as "protojets" in the jet clustering.

4.3 Data samples and event selection

The pp data used in this thesis were taken during LHC proton-proton collisions at $\sqrt{s} = 5.02$ TeV. The integrated luminosity of 25 pb^{-1} was collected between 19th of November 2015 and 24th of November 2015. The collision data were required to satisfy the good run list which ensures stable beams and fully operational ATLAS detector. Events were collected using the dimuon trigger which requires two oppositely charged muons with $p_T > 4$ GeV [34]. In total 37634508 events were used for the study in this thesis.

Muon candidates are required to pass the "Tight working point"[1] as well as the following criteria [34]:

- $p_T > 4$ GeV and $|\eta| < 2.4$;
- pixel hits + pixel dead sensors > 0;
- SCT hits + SCT dead sensors > 4;
- pixel holes + SCT holes < 3;
- for $0.1 < |\eta| < 1.9$, $n_{\mathrm{TRT}}^{\mathrm{hits}} + n_{\mathrm{TRT}}^{\mathrm{outliers}} > 5$ and $n_{\mathrm{TRT}}^{\mathrm{outliers}} < 0.9(n_{\mathrm{TRT}}^{\mathrm{hits}} + n_{\mathrm{TRT}}^{\mathrm{outliers}})$
- the selected muon must be matched with trigger elements within a cone of $\Delta R < 0.01$ from the trigger candidate.

Here hit represents a signal in one channel of a given tracking subdetector and outlier represents a signal which is distant with respect to an expectation from the fit procedure. The two muons in the pair which constitute a charmonium candidate are required to originate from a common vertex. The charmonium candidate is required to have invariant mass in the interval of $2.9 - 3.1$ GeV. No correction on tracking efficiency and acceptance are applied, but for a given kinematic selection, those were shown to vary only weakly with changing p_T and η [34].

Jets used in the data were reconstructed using the anti-k t algorithm with R = 0.4 with a dedicated underlying event subtracion [37] which prevents jets for being distorted by the presence of large underlying event of a heavy-ion collision.

[1] Working point is a set of requirements imposed on signal in ID and muon system which ensure high probability for a muon candidate to be the actual muon while ensuring minimal loss of candidates due to requiring restrictive cuts (that is while keeping a high efficiency for the muon reconstruction [35, 36])

Chapter 5

Results

In this chapter we will present the original results of this thesis. Results are divided into four sections in this chapter. First section describes several tests of the MC generator: comparison of several different PDF settings and study of the role of ISR and/or FSR. In the second section, we compare MC output against the actual results published by ATLAS. The third and fourth sections show a study of correlation of charmonia production and jet production in MC and ATLAS data, respectively.

5.1 Tests of different PYTHIA settings

First of all, we have run PYTHIA with the most natural settings of QCD - all hard processes enabled. This approach yielded no useful results, as less than 50 charmonia were produced in 10^6 of collisions. This is due to charm quarks large mass compared to up and down quarks. Therefore we have restricted PYTHIA to channels producing charmonia (actual PYTHIA setting are described in Section 4.2).

In the first test, we were comparing three of the most commonly used PDF sets - CT10nlo [38], MSTW2008 [39] and NNPDF2. 3 [40]. It is apparent from the following results, that we can neglect the effect of different PDF sets and use only one. For this purpose we have chosen CT10nlo since it is often used as a default setting. Upper panel of Figure 5.1 shows rapidity distribution for J/ψ for above specified three PDF sets. As expected, the distribution has gaussian shape. Next, lower panel of Figure 5.1 shows ratio between CT10nlo and other PDF sets.

Another important comparison is a comparison of ISR and FSR setting, which allows to observe impact of the pre/post-collision emission. This setting has visible impact on the results as will be shown later. Figure 5.2 shows rapidity distribution for CT10nlo PDF set for different radiation settings. The distribution is again gaussian as we have expected. From these two figures it is apparent, that radiation or PDF sets have no effect on the rapidity distribution of J/ψ. In the next section we will show that PDF sets does not effect the shape of the cross-section for J/ψ production evaluated as a function of p_T, but different settings of radiations can change results rather dramatically.

Figure 5.3 shows comparison of transverse momentum for charmonia for different radiation settings. The non-uniform binning was chosen to match the

published results by ATLAS [32].

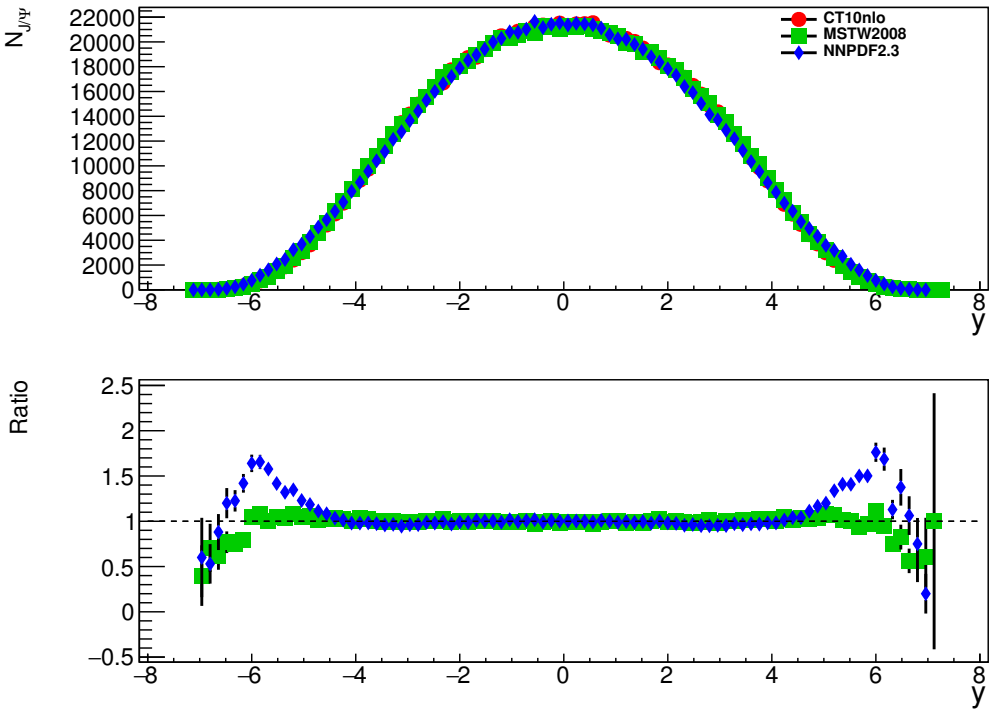

Figure 5.1: Top: Comparison of rapidity distributions of J/ψ for three different PDF sets: CT10nlo, MSTW2008 and NNPDF2. 3 with default PYTHIA settings. Bottom: Ratio of MSTW2008 and NNPDF2. 3 PDFs with respect to CT10nlo.

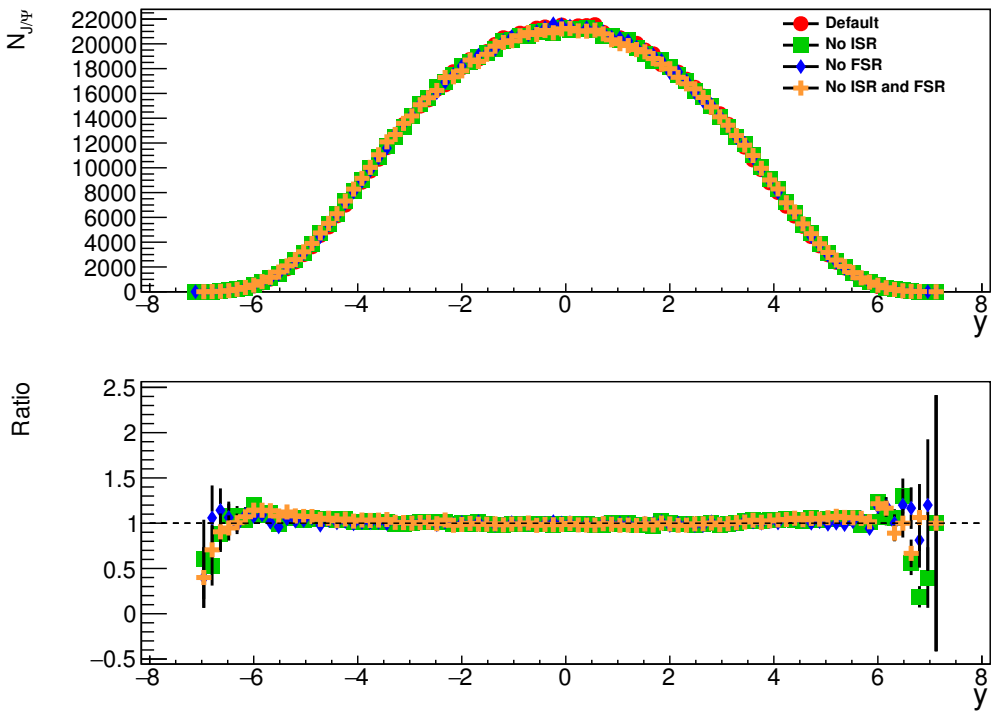

Figure 5.2: Top: Comparison of rapidity distributions of J/ψ for CT10nlo PDF set with different radiation settings: red - default settings (both ISR and FSR turned on), green - ISR turned off, blue - FSR turned off, yellow - both ISR and FSR turned off. Bottom: Ratio of various radiation setting compared to the default one.

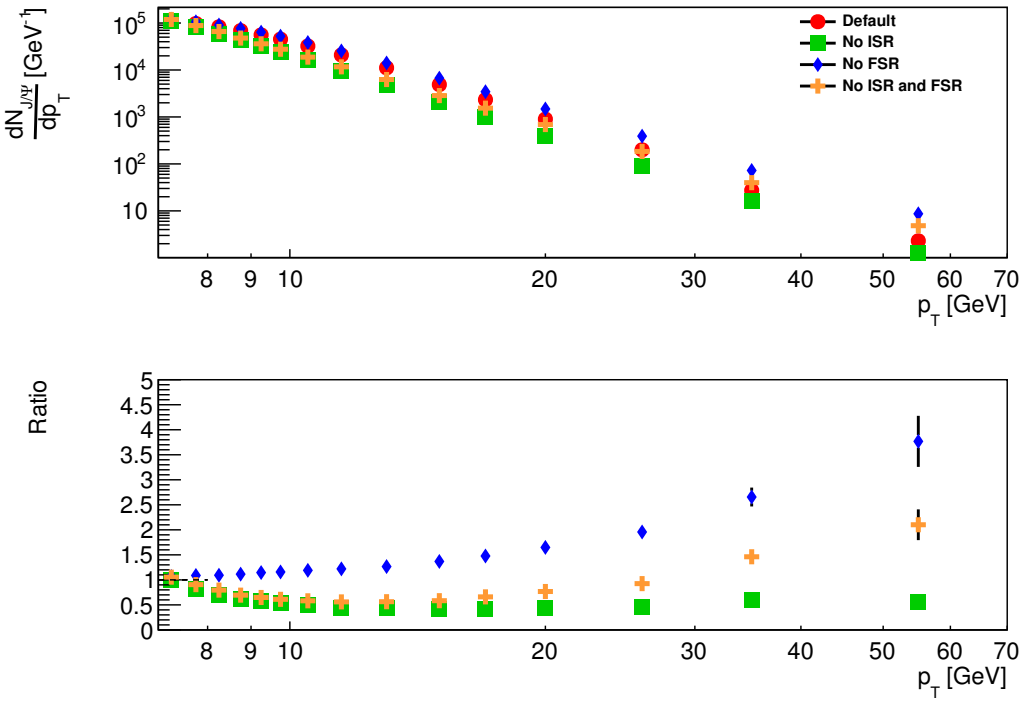

Figure 5.3: Top: Comparison of p_T distributions for J/ψ for different radiation settings for CT10nlo PDF set: red - default setting (both ISR and FSR turned on), green - ISR turned off, blue - FSR turned off, yellow - both ISR and FSR turned off. Bottom: Ratio of various radiation setting compared to the default one).

5.2 PYTHIA to data comparison

In this section, we will compare results from PYTHIA MC generator with data measured by ATLAS [32]. We will be using rapidity cut on J/ψ of $|y| < 0.75$.

Figure 5.4 shows p_T distribution of charmonia for three different PDF sets as well as results by ATLAS. We have normalized all PYTHIA data to the first bin of the ATLAS. We have done so, to compare shapes of the distributions, rather than absolute values. As one can see from the bottom panel of Figure 5.4 the choice of PDF has only moderate impact on the cross-section. The difference among three different PDF sets is smaller then 20%. Thus the variation in the choice of PDF cannot cover for a difference in the shape of the cross-section seen between the data and MC.

Figure 5.5 compares differential cross-section by ATLAS to different radiation setting of PYTHIA for CT10nlo PDF set (all other PDF sets yield same results and are not shown here). Interestingly, most unnatural setting with no ISR and no FSR fits the data the best.

The evaluation of the ratio between ATLAS data and PYTHIA MC is unfortunately not possible since in the case of the ATLAS data, the cross-section is not evaluated in the center of the bin but it is evaluated in the barycenter of the bin. In order to quantify the impact of these two different approaches we have evaluated the normalized cross-section from PYTHIA also in the barycenter of the bin and compared it with the cross-section evaluated in the bin center. The impact is significant as one can see in Figure 5.6.

Comparison of absolute cross-sections between data and PYTHIA was also done and the cross-section in MC was found to be 10^3 higher compared to that reported by ATLAS. While it is well known that the description of the charmonia production by PYTHIA is not very precise, such a large difference is unexpected. However, we did not identify any problem with the overall normalization of the MC samples which would explain this difference.

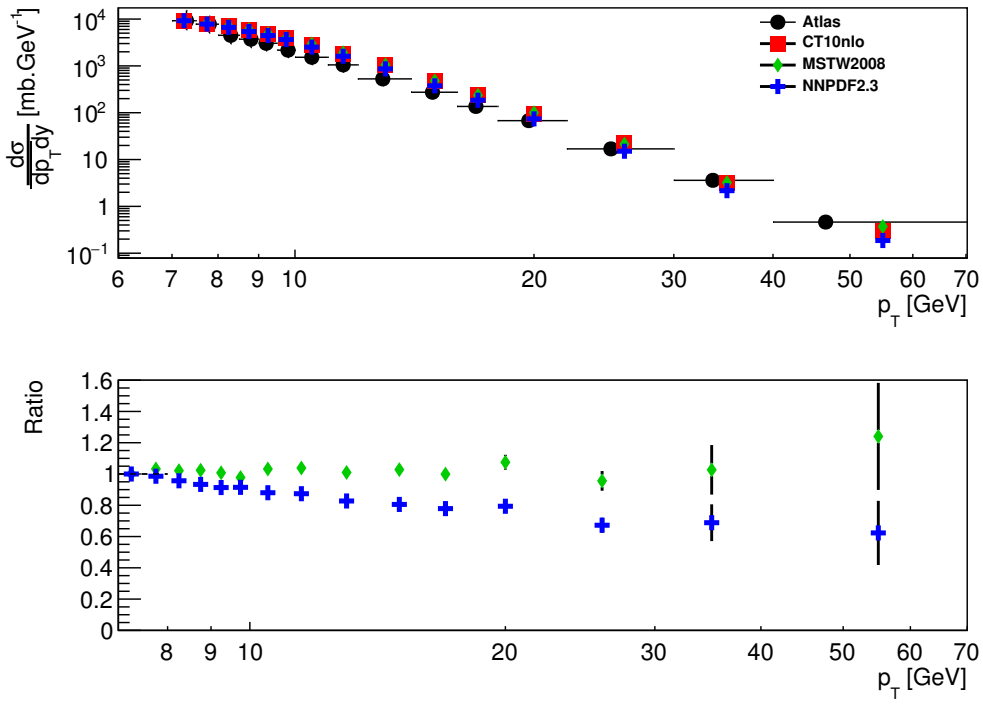

Figure 5.4: Top: Differential cross-section for J/ψ production for rapidity cut $|y| < 0.75$ evaluated as function of p_T. Vertical error bars represent statistical uncertainties and horizontal error bars represent the width of the bin. PYTHIA cross-section is normalized such that its value in the first bin matches the value in the cross-section in the first bin in the data. For ATLAS data, vertical error bars represent combined statistical and systematical uncertainties. Bottom: Ratio of MSTW2008/NNPDF2.3 PDFs with respect to CT10nlo.

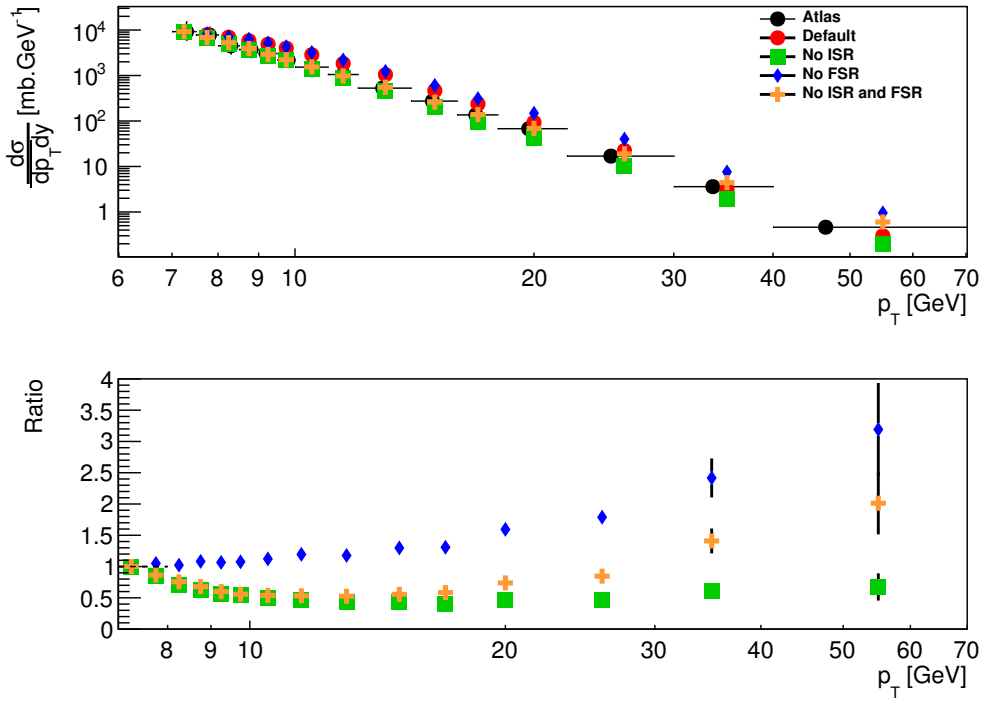

Figure 5.5: Top: Differential cross-section for J/ψ production for rapidity cut $|y| < 0.75$ evaluated as function of p_T. PYTHIA cross-section is normalized such that its value in the first bin matches the value in the cross-section in the first bin in the data. Vertical error bars represent statistical uncertainties and horizontal error bars represent the width of the bin. For ATLAS data, vertical error bars represent combined statistical and systematical uncertainties. Bottom: Ratio of various radiation setting compared with the default one (where both ISR and FSR are enabled).

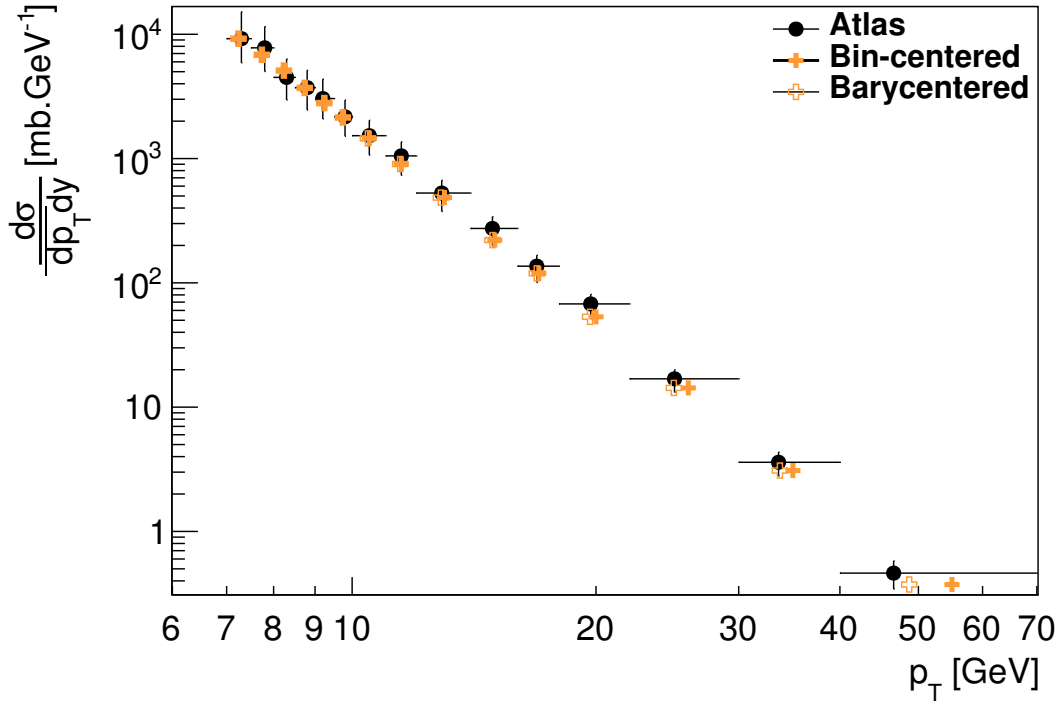

Figure 5.6: Cross-section for the inclusive J/ψ production as a function of p_T for default PYTHIA configuration compared with data by ATLAS. PYTHIA cross-section is normalized such that its value in the first bin matches the value in the cross-section in the first bin in the data.

5.3 Charmonia in jets in MC

In this section we will present results of the study of the correlation of charmonia and jet production. The goal of this study is to quantify how many charmonia are created within jets and how many jets contain charmonia. As we saw in the two previous sections, the choice of PDF set does not impose any important differences, so we will restrict ourselves to only one set - CT10nlo as argued before.

For this study, we have introduced two observables, namely ρ_{jet} and ρ_{charm}, defined as follows:

$$\rho_{jet} = \frac{N_{jet}^{J/\psi}}{N_{jet}^{all}} \tag{5.1}$$

and

$$\rho_{J/\psi} = \frac{N_{J/\psi}^{jet}}{N_{J/\psi}^{all}}, \tag{5.2}$$

where $N_{jet}^{J/\psi}$ is the number of jets with charmonium, N_{jet}^{all} is number of all jets, $N_{J/\psi}^{jet}$ is number of charmonia with jets and $N_{J/\psi}^{all}$ is number of all charmonia.

Charmonia are associated with jets based on a spacial matching with the requirement of $\Delta R < 0.4$, where ΔR is the distance in the $\eta - \phi$ space between the jet axis and the position of J/ψ.

Distributions of observales defined in Equations (5.1) and (5.2) are show on Figures 5.7 and 5.8, respectively. For both figures we have taken only jets with $p_T^{jet} > 5$GeV and left all charmonia with no restrictions.

We have investigated two configurations in greater detail - Default configuration, as it is the default configuration for the MC generator, and configuration without ISR and without FSR as well, as this was the configuration that matched the data in section 5.2 the best. Figures 5.9 and 5.10 show the default configuration and Figures 5.11 and 5.12 refer to the the configuration with no ISR ano no FSR. In the following paragraphs we will describe the results of Figures 5.7 - 5.12 in more details

Figure 5.7 shows that the fraction of jets with J/ψ is generally smaller then 4% in the MC. This fraction increases from 1% to higher values with increasing p_T of the jet. Configurations with no ISR and no FSR clearly suppress the events with charmonia produced within jets. Figure 5.8 shows that the production of charmonia in jets is connected with larger values of charmonia p_T, since below $p_T^{J/\psi}$ of 15 GeV the $\rho_{j/\psi}$ is negligible. To further quantify the correlation between jets and charmonia production, Figures 5.9 and 5.10 show 2D distributions of ρ_{jet} and $\rho_{j/\psi}$ evaluated as a function of both, p_T^{jet} and $p_T^{J/\psi}$. One can see that large values of ρ are connected with large values of p_T^{jet} and $p_T^{J/\psi}$. Figure 5.9 and 5.10 show also "profiles" along the x-axis, that is the ρ_{jet}-weighted average value of $p_T^{J/\psi}$ for a given value of p_T^{jet} and $\rho_{J/\psi}$-weighted average value of p_T^{jet} for a given value of $p_T^{J/\psi}$, respectively. The profile on Figure 5.9 shows an increase of average value of $p_T^{j/\psi}$ with increasing p_T^{jet} while the complementary profile on Figure 5.10 does not show such an increasing trend. These trends reflect the fact that the jet production associated with J/ψ in PYTHIA largely results from ISR and FSR. These radiation processes are connected with the hard process (ISR) and the color non-singlet state of resonance of excited charmonium "decaying" to the stable, color-singlet J/ψ state (FSR). The correlation of large ρ with FSR

and ISR is also quantified in Figures 5.11 and 5.12. With no FSR and ISR jet p_T is in general not greater than 10-20 GeV.

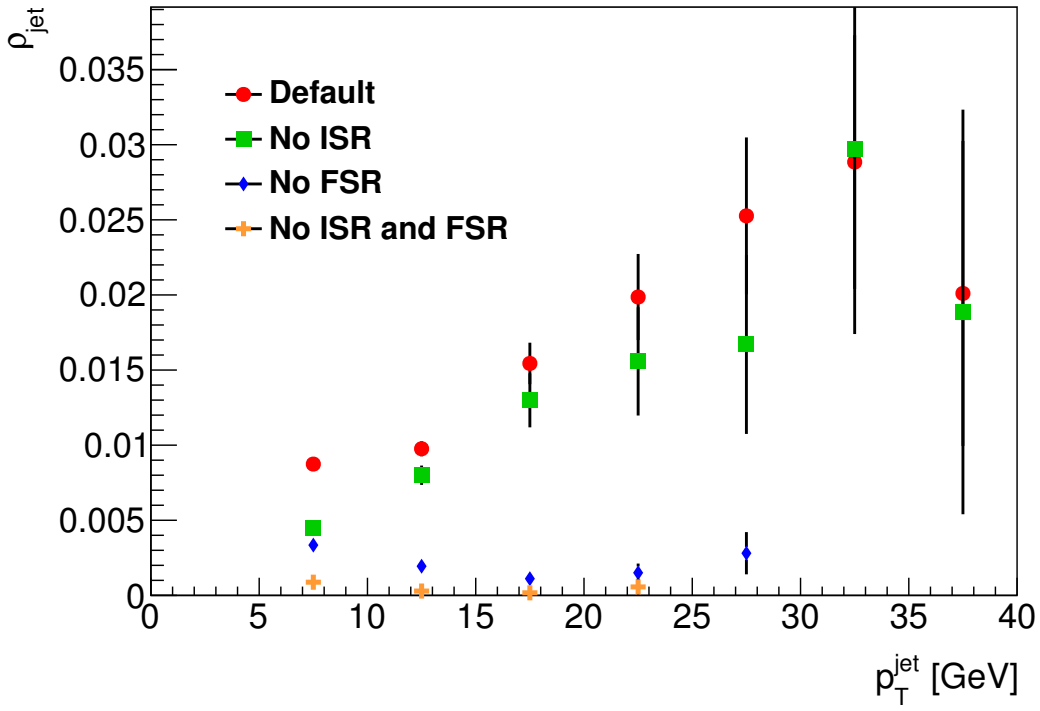

Figure 5.7: Fraction of jets with J/ψ in PYTHIA MC. Default configuration (red), configuration with no ISR (green), configuration with no FSR (blue), and configuration for which both the ISR and FSR are turned off (yellow).

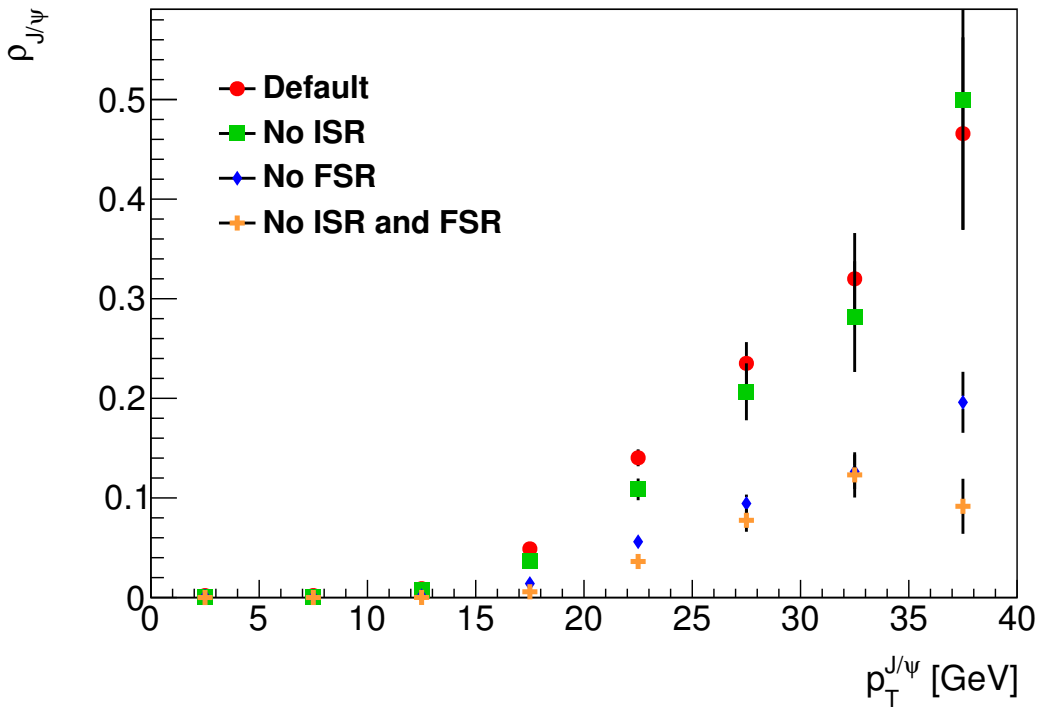

Figure 5.8: Fraction of J/ψ with jets in PYTHIA MC. Default configuration (red), configuration with no no ISR (green), configuration with no FSR (blue), and configuration for which both the ISR and FSR are turned off (yellow).

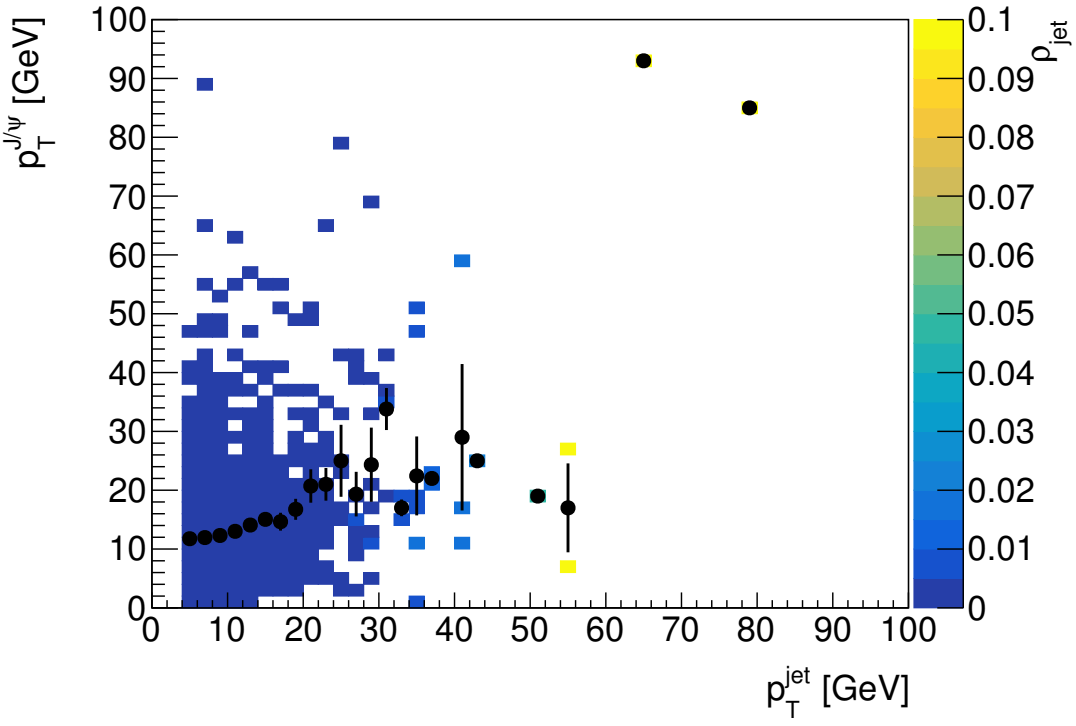

Figure 5.9: 2D histogram representing fraction of jets with J/ψ in PYTHIA MC for default PYTHIA configuration with ISR and FSR turned on. Black markers represent average value of $p_T^{J/\psi}$ for a given value of p_T^{jet}.

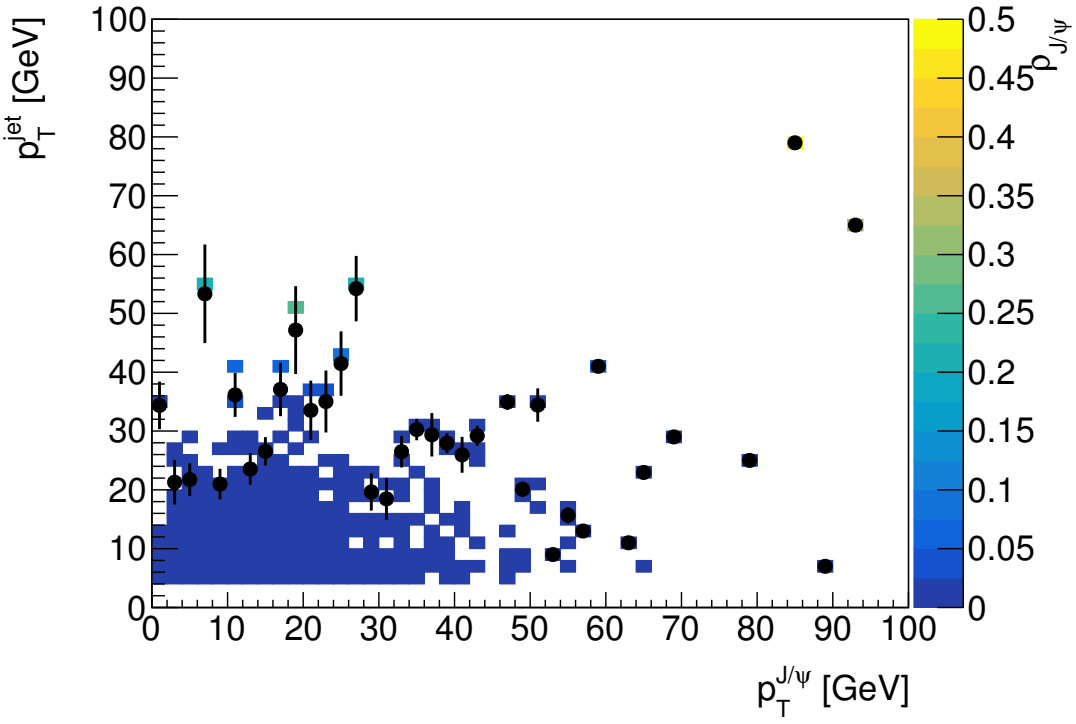

Figure 5.10: 2D histogram representing fraction of J/ψ with jets in PYTHIA MC for default PYTHIA configuration with ISR and FSR turned on. Black markers represent average value of p_T^{jet} for a given value of $p_T^{J/\psi}$.

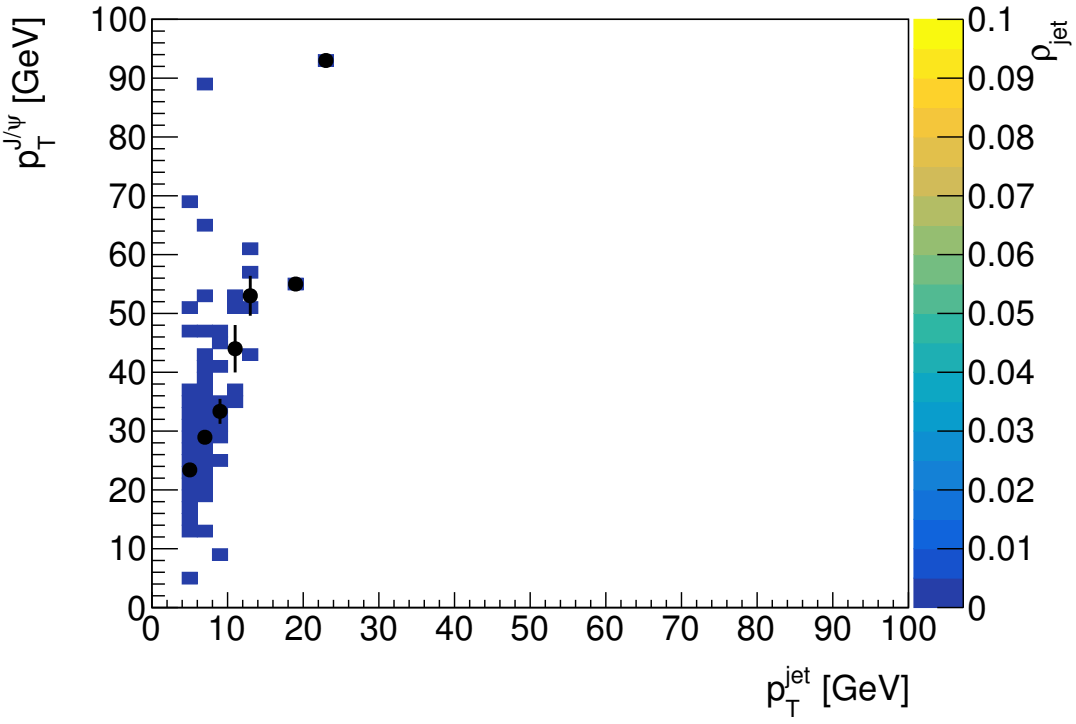

Figure 5.11: 2D histogram representing fraction of jets with J/ψ in PYTHIA MC for ISR and FSR turned off. Black markers represent average value of $p_T^{J/\psi}$ for a given value of p_T^{jet}.

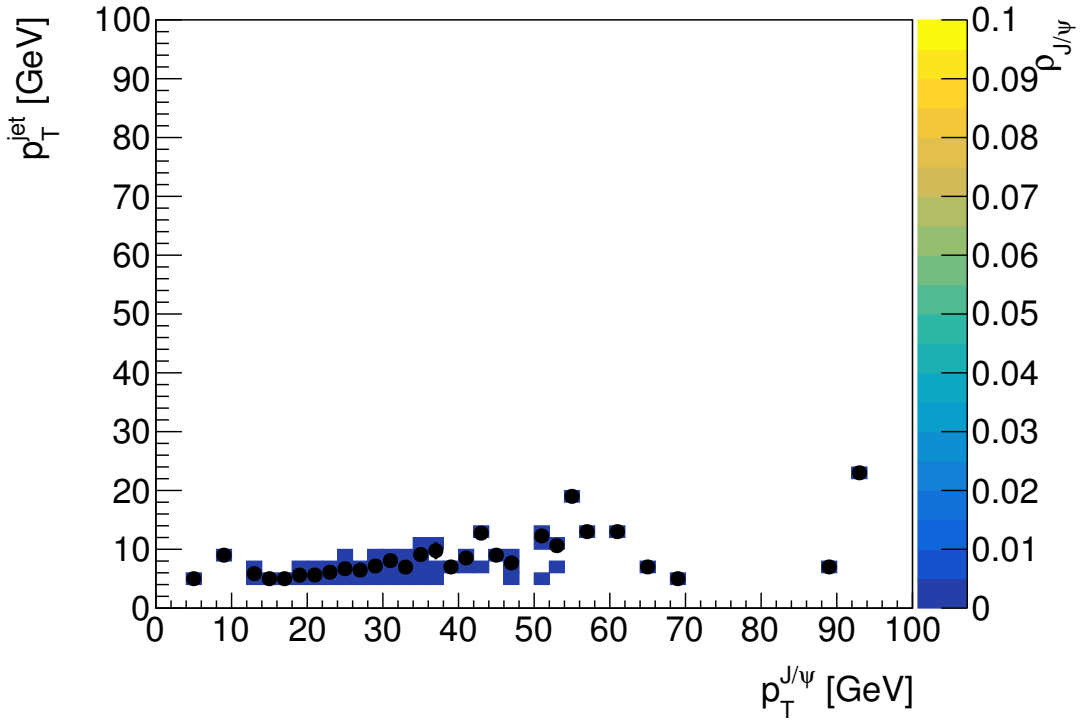

Figure 5.12: 2D histogram representing fraction of J/ψ with jets in PYTHIA MC with ISR and FSR turned off. Black markers represent average value of p_T^{jet} for a given value of $p_T^{J/\psi}$.

5.4 Charmonia in jets in data

This section presents the same observables as defined in the previous section but now for the pp data described in Section 4.3. While the reconstruction of J/ψ signal in MC is simple, it is much more difficult in the data since the detector cannot directly measure the J/ψ particle due to its fast decay. To find charmonia, we have evaluated the invariant mass of all the muon pairs in the event. This invariant mass is shown in Figure 5.13. As can be seen, significant peak is visible in the region around 3.1 GeV, which can be safely connected with J/ψ. To calculate the background of the peak, we have used an rectangle spanning from 2.9 GeV to 3.1 GeV with height equal to average of the height of the left and right ends. The full peak area(with background) is 64 GeV^{-1} and background is equal to 12.8 GeV^{-1}. In Figure 5.14 we show the observable $\rho_{J/\psi}$ defined in Equation

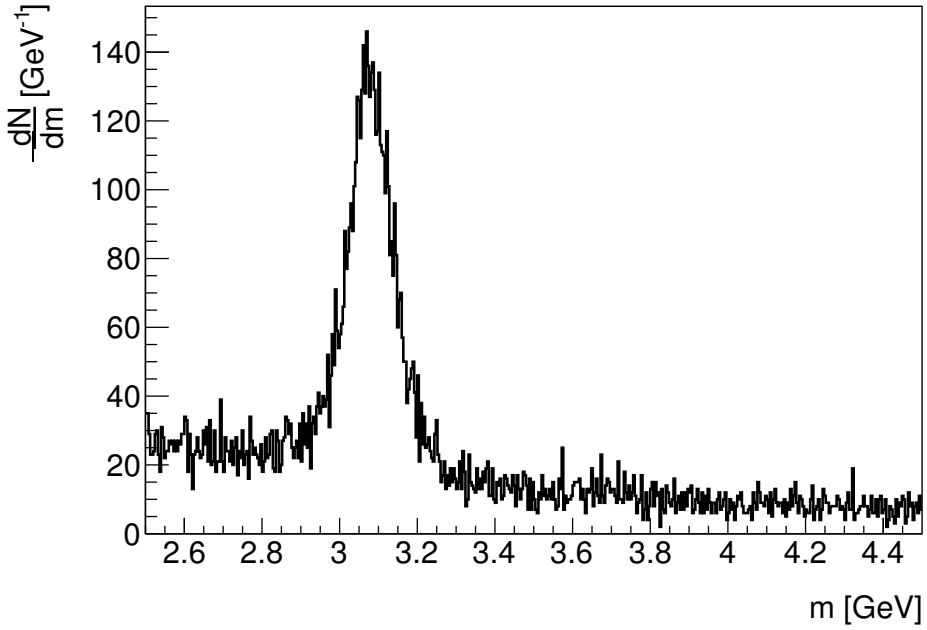

Figure 5.13: Invariant mass of muon pairs calculated from data.

(5.2) for p_T of all muon pairs with invariant mass between 2.9 and 3.1 GeV. Figure 5.15 presents the same quantity but in grater detail - in 2D histogram.

To see if the charmonia are correlated with jets, we took muons of invariant mass between 3.6 and 4.4 GeV (which is pure background as can one see in Figure 5.13). These muon pairs do not represent J/ψ meson. Results are in Figures 5.16 and 5.17.

The fraction of J/ψ with jets in the signal region does not exceed 10% and it is in general smaller in the data than in MC. Rather surprising is the fact that the fraction of muon pairs associated with jets in the background region is comparable to that in the signal region. This might be a result of a trigger bias, since the sample containing muon triggers contained also jet triggers. Irrespective of that, these results imply that J/ψ with p_T of $5 - 40$ GeV in the data is not predominantly produced along with a jet. This represents an important, original result of this study.

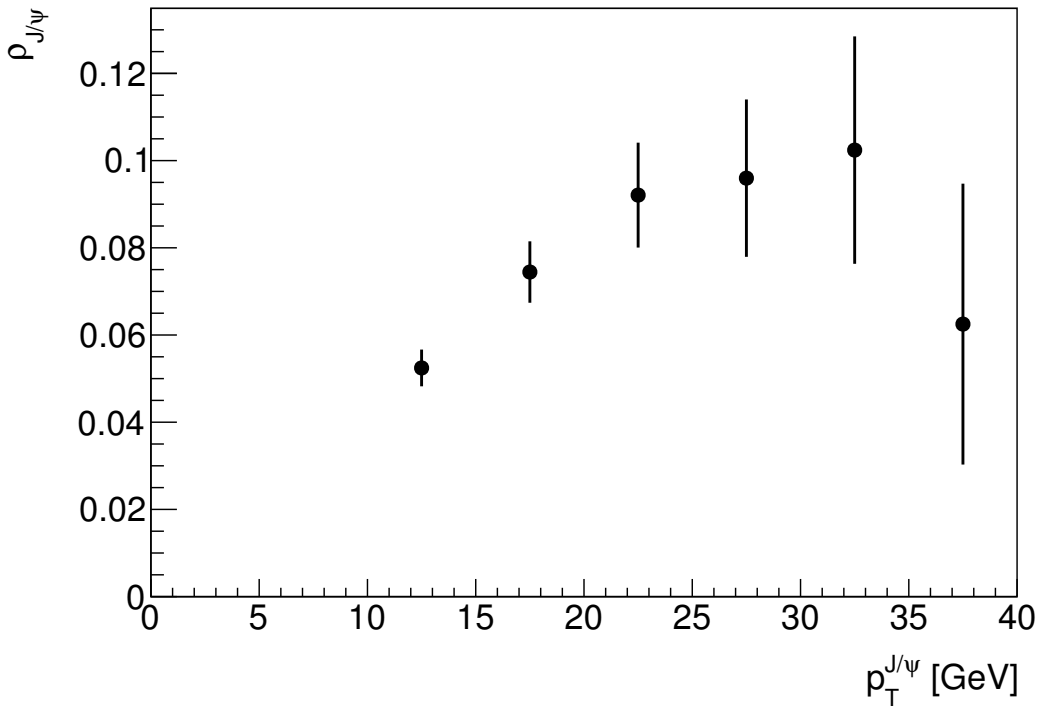

Figure 5.14: $\rho_{J/psi}$ observable as a function of $p_T^{J/\psi}$ computed from muon invariant mass pairs between 2.9 and 3.1 GeV with jets in ATLAS data.

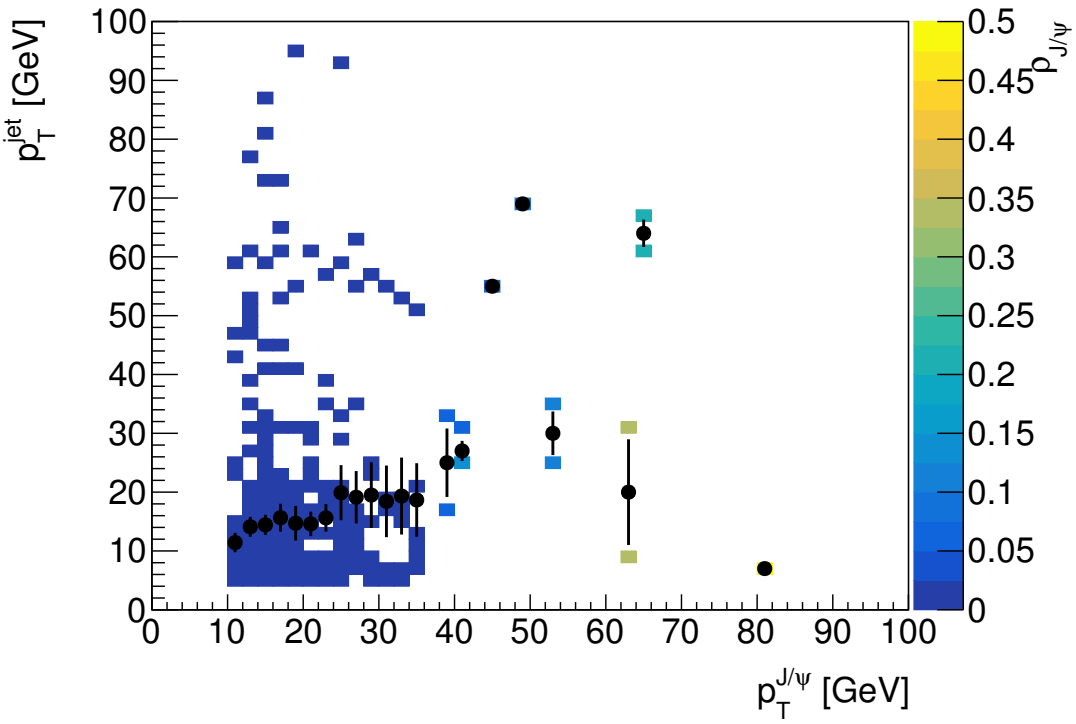

Figure 5.15: 2D histogram representing fraction of muon invariant mass pairs between 2.9 and 3.1 GeV with jets in ATLAS data. Black markers represent average value of p_T^{jet} for a given value of $p_T^{J/\psi}$.

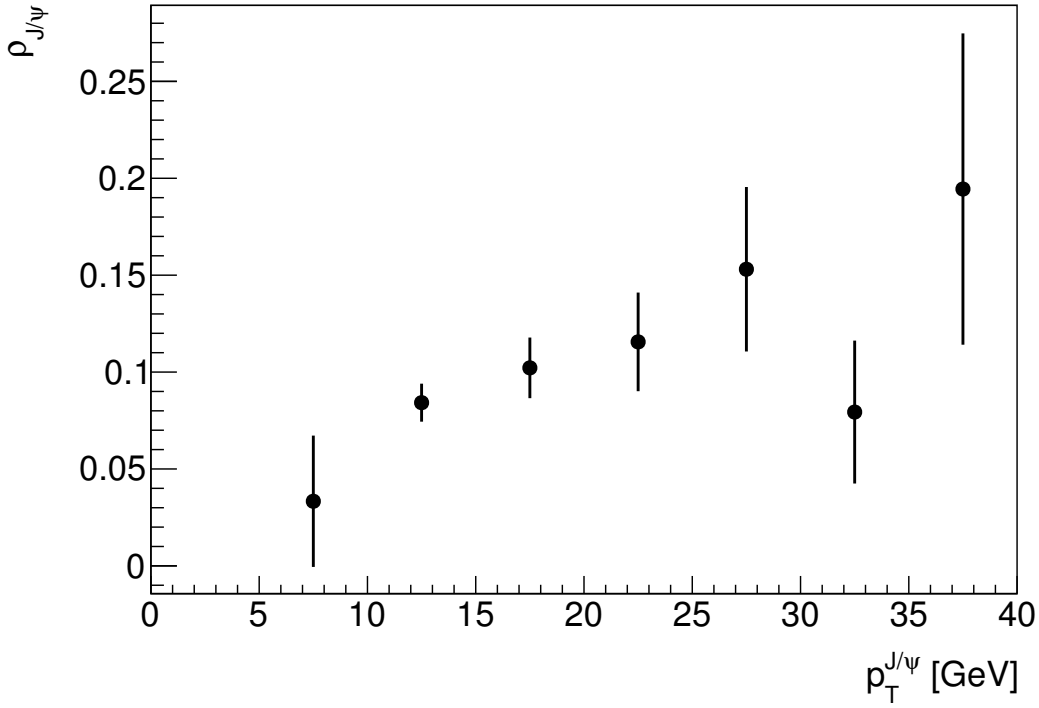

Figure 5.16: $\rho_{J/psi}$ observable as a function of $p_T^{J/\psi}$ computed from muon invariant mass pairs between 3.6 and 4.4 GeV with jets in ATLAS data.

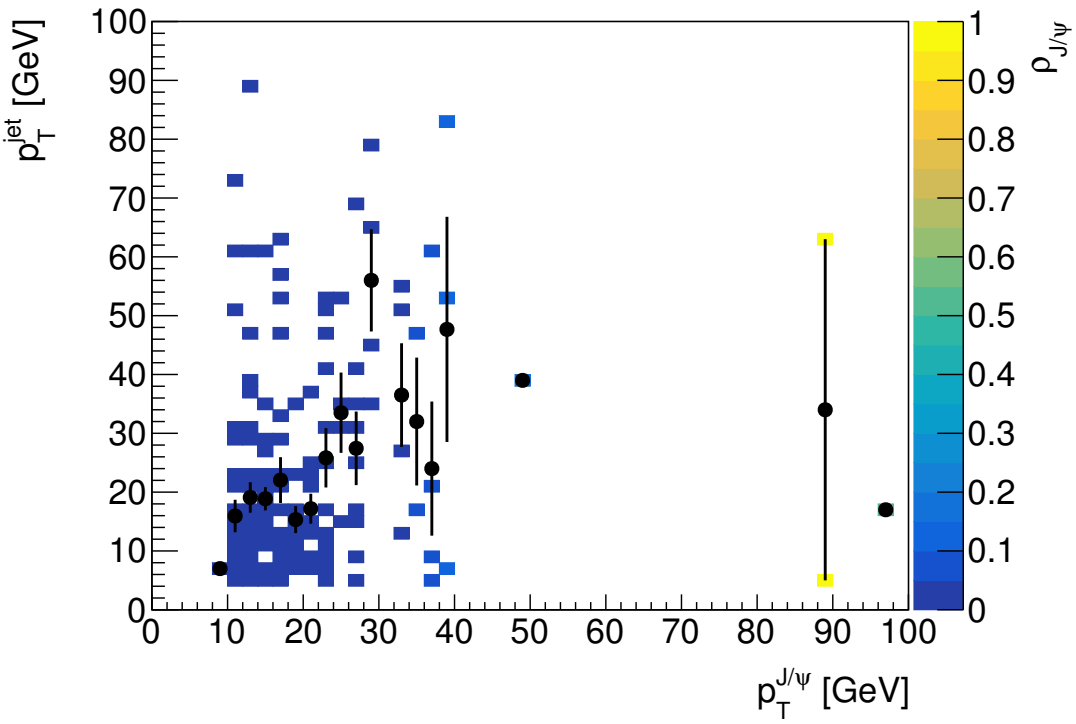

Figure 5.17: 2D histogram representing fraction of muon invariant mass pairs between 3.6 and 4.4 GeV with jets in ATLAS data. Black markers represent average value of p_T^{jet} for a given value of $p_T^{J/\psi}$.

Chapter 6

Conclusions

In this thesis we have introduced the reader to the problematics of the charmonia and jet production in proton-proton and heavy-ion collisions. After the introduction to strong interaction and heavy-ion collisions in Chapter 1 and 2, respectively, and after Chapter 3 which described the LHC and ATLAS experiment, we have concentrated on original results of this work. First, we have described data and MC samples used in the study in Chapter 4 and the results are shown in Chapter 5.

The main goal of the thesis was to explore the charmonia production and in particular its correlation with the production of jets. We have compared basic distributions such as the rapidity distribution and the differential cross-section for the J/ψ production between MC simulation from PYTHIA and data measured by ATLAS at the LHC. The results show that basic observables in MC are not sensitive to the choice of parton distribution functions. On the other hand, initial and final state radiation have sizable impact on the distributions under the study. The configuration best fitting the data was that with both initial and final state radiation turned off. Next we have quantified the correlation between the production of jets and J/ψ. Jets were reconstructed using the anti-k_t algorithm with $R = 0.4$ using the FastJet library. We have found that on average, only few percent of jets contain a J/ψ particle in the case of the PYTHIA simulation. On the contrary, at high-p_T of J/ψ as much as half of J/ψ has an associated jet. These MC results can be contrasted with results from data where we found that only up to 10% of charmonia with p_T in the range of $5 - 40$ GeV can can be associated with a jet. This represents an important, original result, which, to our knowledge, was not published in the literature.

While the understanding of the charmonia production is crucial in the context of charmonium suppression in heavy-ion collisions, this thesis did not reach to the analysis of data from heavy-ion collisions. It would be useful to perform a similar study, perhaps with more sophisticated identification of charmonia, in heavy-ion collisions.

Bibliography

[1] Jiri Horejsi. *Fundamentals of Electroweak Theory.*

[2] Standard Model Wikipedia. [online], Last visited at 21.4.2018. https://en.wikipedia.org/wiki/Standard_Model.

[3] J. I. Friedman. Peering inside the proton. *Eur. Phys. J.*, H36:469–485, 2012.

[4] Michael E. Peskin Daniel V. Schroeder. *An Introduction to Quantum Field Theory.* 1995.

[5] C. Patrignani et al. Review of Particle Physics. *Chin. Phys.*, C40(10):100001, 2016.

[6] H. David Politzer. Reliable Perturbative Results for Strong Interactions? *Phys. Rev. Lett.*, 30:1346–1349, 1973. [,274(1973)].

[7] David J. Gross and Frank Wilczek. Ultraviolet Behavior of Nonabelian Gauge Theories. *Phys. Rev. Lett.*, 30:1343–1346, 1973. [,271(1973)].

[8] Jiri Chyla. *Quarks, partons and Quantum Chromodynamics.*

[9] Matteo Cacciari, Gavin P. Salam, and Gregory Soyez. The anti-k_t jet clustering algorithm. *JHEP*, 04:063, 2008.

[10] S. Catani, Yuri L. Dokshitzer, M. H. Seymour, and B. R. Webber. Longitudinally invariant K_t clustering algorithms for hadron hadron collisions. *Nucl. Phys.*, B406:187–224, 1993.

[11] Stephen D. Ellis and Davison E. Soper. Successive combination jet algorithm for hadron collisions. *Phys. Rev.*, D48:3160–3166, 1993.

[12] Yuri L. Dokshitzer, G. D. Leder, S. Moretti, and B. R. Webber. Better jet clustering algorithms. *JHEP*, 08:001, 1997.

[13] Martin Spousta. The influence of the underlying event on jet measurements in heavy ion collisions. *J. Phys. Conf. Ser.*, 270:012013, 2011.

[14] S. L. Glashow, J. Iliopoulos, and L. Maiani. Weak Interactions with Lepton-Hadron Symmetry. *Phys. Rev.*, D2:1285–1292, 1970.

[15] CERN Heavy Ion Collisions. [online], Last visited at 21.4.2018. https://home.cern/about/physics/heavy-ions-and-quark-gluon-plasma.

[16] Mischke QGP-Alice Group. Research. [online], Last visited at 21.4.2018. http://www.staff.science.uu.nl/ misch101/research.htm.

[17] A. Adare et al. Trends in Yield and Azimuthal Shape Modification in Dihadron Correlations in Relativistic Heavy Ion Collisions. *Phys. Rev. Lett.*, 104:252301, 2010.

[18] Geoffrey T. Bodwin, Eric Braaten, and G. Peter Lepage. Rigorous QCD analysis of inclusive annihilation and production of heavy quarkonium. *Phys. Rev.*, D51:1125–1171, 1995. [Erratum: Phys. Rev.D55,5853(1997)].

[19] Martin Spousta. On similarity of jet quenching and charmonia suppression. *Phys. Lett.*, B767:10–15, 2017.

[20] ATLAS Collaboration. Observation of a Centrality-Dependent Dijet Asymmetry in Lead-Lead Collisions at $\sqrt{s_{NN}} = 2.77$ TeV with the ATLAS Detector at the LHC. *Phys. Rev. Lett.*, 105:252303, 2010.

[21] Michael L. Miller, Klaus Reygers, Stephen J. Sanders, and Peter Steinberg. Glauber modeling in high energy nuclear collisions. *Ann. Rev. Nucl. Part. Sci.*, 57:205–243, 2007.

[22] R. J. Glauber. Cross-sections in deuterium at high-energies. *Phys. Rev.*, 100:242–248, 1955.

[23] Roger D. Woods and David S. Saxon. Diffuse Surface Optical Model for Nucleon-Nuclei Scattering. *Phys. Rev.*, 95:577–578, 1954.

[24] Morad Aaboud et al. Prompt and non-prompt J/ψ and $\psi(2S)$ suppression at high transverse momentum in 5.02 TeV Pb+Pb collisions with the ATLAS experiment. 2018.

[25] Cern homepage. [online], Last visited at 21.4.2018. https://home.cern.

[26] ATLAS detector description webpage. [online], Last visited at 21.4.2018. http://atlas.cern/discover/detector.

[27] LHC Wikipedia. [online], Last visited at 21.4.2018. https://en.wikipedia.org/wiki/Large_Hadron_Collider.

[28] Django Manglunki. LHC Injectors. [online], Last visited at 21.4.2018. https://home.cern/cern-people/updates/2016/11/lhc-report-role-injectors.

[29] Georges Aad et al. Observation of a new particle in the search for the Standard Model Higgs boson with the ATLAS detector at the LHC. *Phys. Lett.*, B716:1–29, 2012.

[30] CMS Collaboration. Observation of a new boson at a mass of 125 GeV with the CMS experiment at the LHC. *Phys. Lett.*, B716:30–61, 2012.

[31] Torbjorn Sjostrand, Stefan Ask, Jesper R. Christiansen, Richard Corke, Nishita Desai, Philip Ilten, Stephen Mrenna, Stefan Prestel, Christine O. Rasmussen, and Peter Z. Skands. An introduction to PYTHIA 8.2. *Comput. Phys. Commun.*, 191:159–177, 2015.

[32] Georges Aad et al. Measurement of the differential cross-sections of inclusive, prompt and non-prompt J/ψ production in proton-proton collisions at $\sqrt{s} =$ 7 TeV. *Nucl. Phys.*, B850:387–444, 2011.

[33] MC15 Job Options. [online], Last visited at 21.4.2018. https://svnweb.cern.ch/trac/atlasoff/browser/Generators/MC15JobOptions.

[34] Q Hu et al. Supporting note for charmonium and bottomonium analyses using 2013 p+Pb data at 5.02 TeV and 2015 p+p data at at 5.02 TeV. Technical Report ATL-COM-PHYS-2014-1051, CERN, Geneva, Aug 2014.

[35] Muon reconstruction performance in early $\sqrt{s}$=13 TeV data. Technical Report ATL-PHYS-PUB-2015-037, CERN, Geneva, Aug 2015. https://cds.cern.ch/record/2047831.

[36] MCP Analysis Guidelines MC15. [online], Last visited at 21.4.2018. https://twiki.cern.ch/twiki/bin/view/AtlasProtected/MCPAnalysisGuidelinesMC15.

[37] ATLAS Collaboration. Measurement of the nuclear modification factor for inclusive jets in Pb+Pb collisions at $\sqrt{s_{\mathrm{NN}}} = 5.02$ TeV with the ATLAS detector. 2018.

[38] Hung-Liang Lai, Marco Guzzi, Joey Huston, Zhao Li, Pavel M. Nadolsky, Jon Pumplin, and C. P. Yuan. New parton distributions for collider physics. *Phys. Rev.*, D82:074024, 2010.

[39] A. D. Martin, W. J. Stirling, R. S. Thorne, and G. Watt. Parton distributions for the LHC. *Eur. Phys. J.*, C63:189–285, 2009.

[40] Richard D. Ball et al. Parton distributions with LHC data. *Nucl. Phys.*, B867:244–289, 2013.